Sub-Nanogram Mass Sensor for In-Liquid Measurement

by
Jianming Chen

B. En. (Honours), University of Electronic Science and Technology, China, 1982
M. En. (honours), University of Electronic Science and Technology, China, 1985

A THESIS SUBMITTED IN PARTIAL FULFILLMENT OF THE REQUIREMENTS FOR THE DEGREE OF MASTER OF APPLIED SCIENCE

in the School
of
Engineering Science

SIMON FRASER UNIVERSITY
December 1995

ISBN 0-612-16830-1

Canada

PARTIAL COPYRIGHT LICENSE

I hereby grant to Simon Fraser University the right to lend my thesis, project or extended essay (the title of which is shown below) to users of the Simon Fraser University Library, and to make partial or single copies only for such users or in response to a request from the library of any other university, or other educational institution, on its own behalf or for one of its usrs. I further agree that permission for multiple copying of this work for scholarly purposes may be granted by me or the Dean of Graduate Studies. It is understood that copying or publication of this work for financial gain shall not be allowed without my written permission.

Title of Thesis/Project/Extended Essay

"Sub-Nanogram Mass Sensor For In-Liquid Mass Measurement"

Author:

(signature)

Jianming CHEN
(name)

December 7, 1995
(date)

Approval

Name: Jianming Chen

Degree: Master of Applied Science

Title of Thesis: Sub-Nanogram Mass Sensor for In-Liquid Measurement

Examining Committee:

Chairman: Dr. Paul Ho

Dr. M. Parameswaran
Senior Supervisor

Dr. Albert M. Leung
Supervisor

Dr. Marek Syrzycki
Supervisor

Dr. Shahram Payandeh
Examiner

Date Approved: December 7, 1995

Abstract

Measuring mass of biological materials is an important topic in the area of medicine and related studies. Typically, biological cells are cultured in liquid medium and hence measuring the mass poses an interesting problem, if in-liquid mass measurement is needed.

This Thesis investigates the possibility of fabricating a mass measurement device using CMOS-compatible micromachining technology. The gate polysilicon available in the commercial CMOS processes is very strain-sensitive and exhibits a gauge factor of 25. Using the gate polysilicon a strain sensitive structure can be fabricated for the above mentioned application. A microcantilever structure formed out of two layers of silicon dioxide sandwiching the strain sensitive polysilicon was designed and fabricated using Northern Telecom's CMOS 3DLM process and MITEL's 1.5 μm Technology. The chips were then anisotropically etched and packaged for experimentation. The mass sensing was accomplished by detecting the shift in the mechanical resonance of the cantilever structure.

The devices were simulated using ANSYS for characterization and performance optimization. An on-chip circuit was also integrated to investigate the feasibility of producing an integrated smart sensor system.

Prototype devices exhibited a mass sensitivity of 25 Hz/ng in air and 23 Hz/ng in DI water respectively. Potential applications and system design will be presented in the Thesis.

to my wife Susan and my daughter Anna

Acknowledgments

I would like to thank my senior supervisor, Dr. Ash Parameswaran for his help, enthusiasm and funding my thesis project. My appreciation goes to the members of the Institute of Micromachine and Microfabrication Research, especially those who have been an inspiration for me. I would like to thank Dr. Albert Leung for his help in the analytical expressions and integrated circuit design, Dr. Marek Syrzycki for his assistance in circuit simulation ideas and Dr. Shahram Payandeh for his help in verifying the model and ANSYS simulation. Thanks to Mr. Ziwei Xie for his help in microfabrication.

I would also like to acknowledge the contribution of Mr. Bill Woods, Mr. Gary Houghton and Dr. Eva Czyzewska in my experiments. Special thanks to all those who helped me with computing systems and lab experiments.

Table of Contents

List of Tables

List of Figures

Chapter 1

Introduction

The technique of using lithographic process and exposing monocrystalline silicon to alkaline chemical etchants to produce concave, pyramidal or other faceted holes, emerged during 1960s and later came known to be the technology of 'bulk micromachining' [1]. This technique was well suited to produce structures such as cantilevers and diaphragms to fabricate functional devices such as acceleration and pressure sensors[2,3].

One other technology that evolved after the bulk micromachining process is the 'surface micromachining' technology[4]. It was assumed that surface micromachining is the suitable technology that can accommodate on-chip circuitry to produce many micromachined transducers. However, a novel technique came into practice which offered designers of the micromachined transducers a unique freedom to design bulk micromachined structures without even using or having access to a complete fabrication facility. This technique is known as CMOS compatible micromachining [5]. This technique, which emerged during late 1980s, allows the integration of micromachined structures and CMOS circuitry on the same chip leading the way to the fabrication of certain micro-electro-mechanical systems [6,7].

A cantilever produced using micromachining technology is a unique structure which offers applications in various areas. Particularly its mechanical characteristics such as applied force versus deflection and mechanical resonant frequency and its dependance to the structure, mass and damping etc., allows the possibility of configuring various sensor and actuator systems using cantilever structure. Further, a cantilever structure is very easy to produce using CMOS compatible micromachining.

In the past few years there is an active research interest in the technique of using mechanical resonance to determine masses of miniature discrete objects [8]. This technique was readily applied to the determination of bio-masses of biological cells. The basic technique in this method of mass measurement is the determination of resonant frequency shift due to mass loading. A cantilever structure is resonated with and without the object of interest and the shift in the resonant frequency is observed. Based on the observed shift in the resonant frequency, the mass can be determined with a resolution of sub-nanogram. The measurement technique utilizes a laser beam that is reflected from the cantilever, usually from the tip of the cantilever. The oscillation amplitude and the frequency is determined by a four quadrant photodiode. This measurement set-up is shown in Figure 1.

The technique mentioned above works extremely well in air and provides excellent signal to noise ratio. Most of the biological objects require a liquid medium in which they can survive. So, the above mentioned technique cannot be applied to measuring masses of biological objects in liquid ambient. Many biological and pharmaceutical experiments need biomass data in liquid ambient and the interest to build a micromachined system to accomplish that became the motivation for this thesis.

Using the CMOS polysilicon as a strain sensitive material, a cantilever could be constructed with the dielectric layers (available in CMOS process) sandwiching a polysilicon resistor. The mechanical deflection of the cantilever structure introduces a strain in the polysilicon. This can be electrically detected as a resistance change. Using this principle, a resonance detection system can be implemented without the use of optical detection technique. This offers a very compact design of mass measurement system with the possibility to integrate on-chip signal conditioning electronics. Most important of all, the cantilever structure could function under a liquid ambient allowing the possibility to determine masses of discrete objects in a liquid medium.

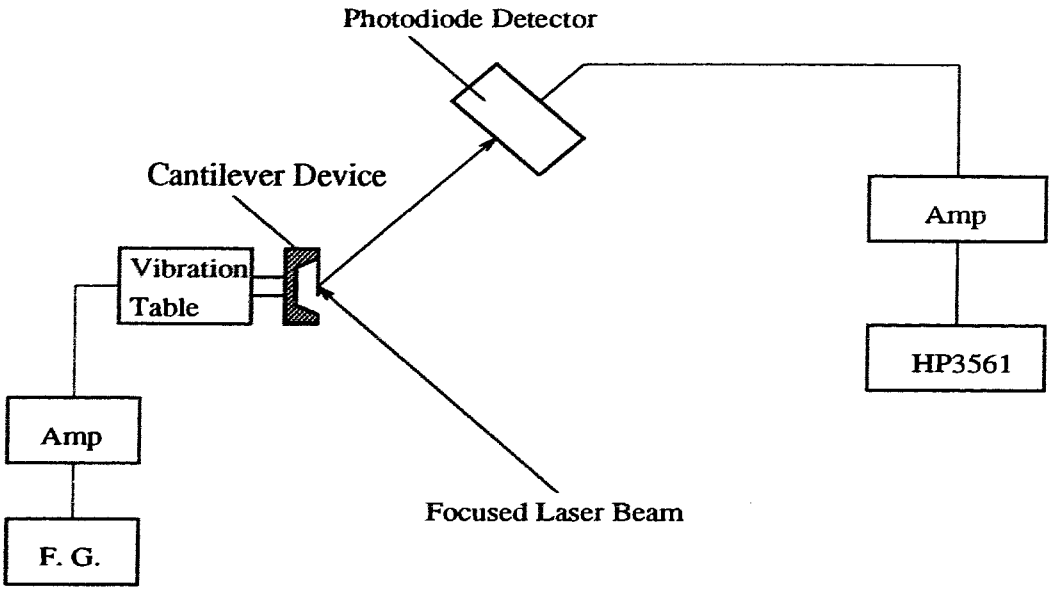

Figure 1: Illustration of optical measurement of resonance

1.1 Thesis Organization

In this Thesis, Chapter 2 outlines the design based on the theory of determination of mass using mechanical resonance and its relevance to the discrete mass sensor. Chapter 3 describes the CMOS compatible micromachining technology and the post processing details to produce the devices. The characterization of piezoresistance coefficients of CMOS polysilicon is presented in Chapter 4. Chapter 5 outlines the experimental mea-

surement set-up. Experimental details and results are explained in chapter 6. Possible applications and several conclusions are drawn in Chapter 7 and Chapter 8, respectively. The details about input and output of ANSYS simulation are given in Appendix A. A brief summary of the theoretical concepts behind piezoresistance is shown in Appendix B.

Chapter 2

Design

The piezoresistive properties of polycrystalline silicon (polysilicon) have been investigated by many researchers [9,10,11]. The literature reports that the CVD polysilicon film has a gauge factor (see page 25 for the definition of the gauge factor) from 10 to 27. For several reasons, this is a very important property of polysilicon in the field of micro-sensors and micro-actuators. First, polysilicon is widely used in CMOS integrated circuits and the well-developed technology exits for depositing and controlling its electrical properties. Hence, it could be easily utilized in integrated sensors. In addition, the polysilicon uses an oxide isolation, thus avoiding the formation of PN junction. This eliminates the leakage problems at higher temperature and makes it ideally suitable for integrated sensors and actuators. Further, the polysilicon can be deposited on a wide range of insulator-coated substrates and its use in MOS technology allows the possibility to integrate MOS circuitry on Si substrates [12].

In modern commercial CMOS processing technology, there are more than one polysilicon layers. One of them is used as the gate material of MOS transistors. The process for depositing this polysilicon layer is well controlled and it has a good quality both in crystal characteristics and in electrical parameters. And the other polysilicon layers are used for capacitors, resistors or interconnects. In my thesis work, the first polysilicon layer (gate material) was selected for the sensitive material because of its electrically stable characteristics. A polysilicon piezoresistor was used to sense a strain. When the strain is induced into the polysilicon, the resistance of the polysilicon will change, and this can be observed using electric means.

2.1 Structural Design of Sensor

2.1.1 Principle

Any solid body has a natural frequency also known as the natural resonant frequency. The resonant frequency is determined by its structure and its mass. If another discrete mass is added on the body, the resonant frequency will change. Based on the shift in the resonant frequency, the mass of the added material can be determined [8]. The lighter the solid body, the more the resonant frequency will shift for the same added mass. Hence, to obtain good sensitivity, it is important to make the structure simple and as light as possible.

The structure for the sensor selected here was a cantilever, which combines two beams to support a pay-load platform, shown Figure 2. A cantilever structure has several advantages: It is a simple design, and offers very low mass for a given shape. During resonance, the free end exhibits maximum displacement and it is easier to detect. Due to two arms support, the cantilever can easily vibrate in longitudinal direction and suppress torsional vibration. Further, the cantilever design requires very short etching time during post-processing.

How to detect the resonant frequency is highly important for a bio-mass sensor to work in-liquid medium. If a strain-sensitive resistor (piezoresistor) is introduced into the resonator, the resistance will change periodically as the resonator is vibrating. When it reaches the resonant point, the amplitude of the vibration is largest, hence, the introduced strain is largest. Consequently, the change of the resistance of the piezoresistor will be largest. It can tell the resonant point. A polysilicon resistor, the gate material in commercial CMOS technology, was added into the cantilever arms to detect its resonant frequency. The resistor was sandwiched inside the multi-layers of the insulators available in CMOS technol-

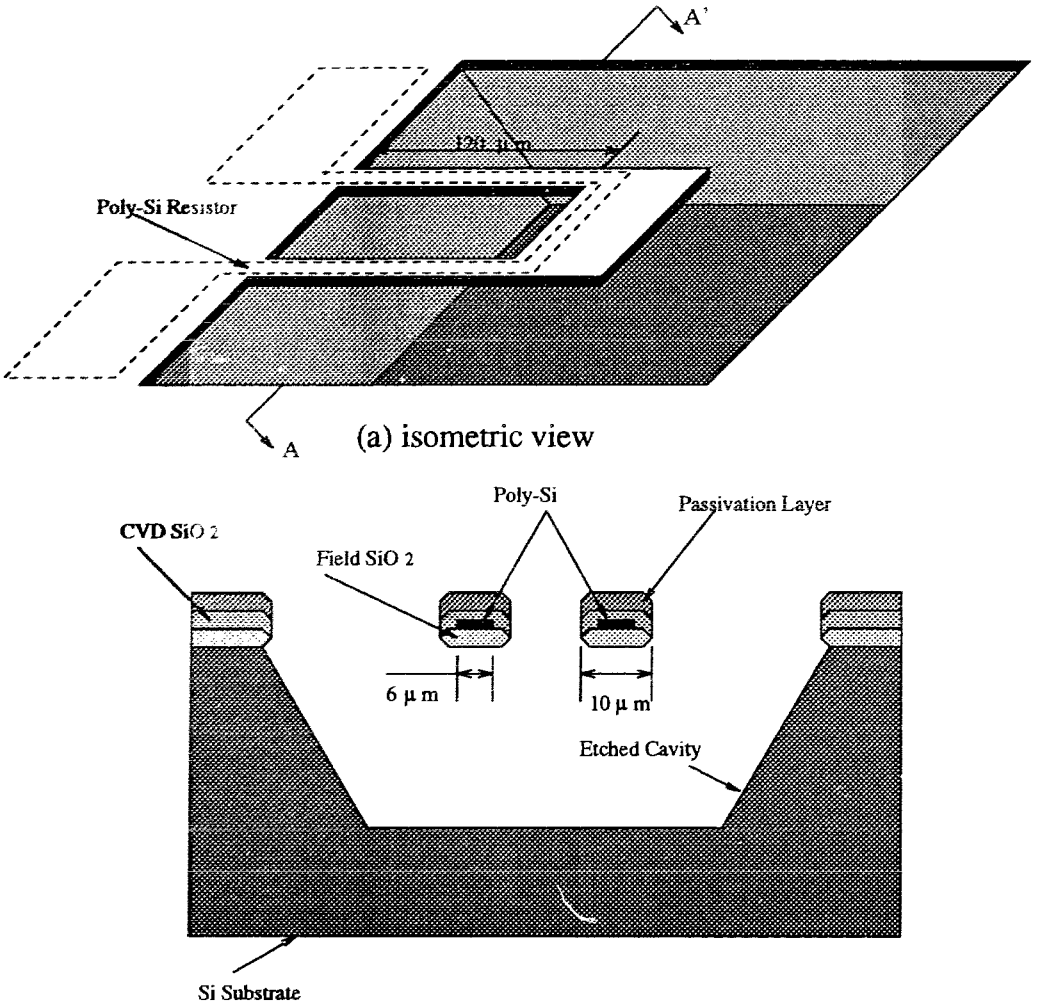

Figure 2: Illustration of the cantilever structure

ogy so that the liquid medium was unable to affect its electrical properties.

2.1.2 Basic Resonant Theory of a Cantilever

A sandwiched cantilever shown in Figure 2 can be considered as an elastic body, and therefore, the elastic resonant theory can be used. In this structure, there are two beams to support a pay-load platform, but this structure can be simulated as a single beam structure, which is as wide as twice of the original beam, supporting a pay-load platform. When a periodic force is applied to the cantilever, it acts as a forced elastic vibrator. Its temporal behavior can be modeled as a damped and forced harmonic oscillator [13]:

$$\frac{d^2Y}{dt^2} + b\frac{dY}{dt} + kY = F_0\cos\omega t \tag{1}$$

where Y is the displacement of the cantilever tip from the equilibrium position, b is the normalized (by the effective mass) damping coefficient, k is the normalized spring constant, and $F_0\cos\omega t$ is the normalized external driving force. One of the solutions of this equation is

$$Y = A(\omega)\cos(\omega t - \theta) \tag{2}$$

The amplitude $A(\omega)$ of the displacement is a function of the frequency of the applied force and can be expressed as

$$A(\omega) = \frac{F_0}{\sqrt{\left((\omega_0)^2 - \omega^2\right)^2 + (b\omega)^2}} \tag{3}$$

where $\omega_0 = \sqrt{k}$ and $f_0 = \omega_0/(2\pi)$, is the resonant frequency for the zero damping $(b = 0)$. If there is damping $(b \neq 0,)$, then the resonant frequency is given by:

$$f_d = \omega_d/(2\pi) = \frac{1}{2\pi}\sqrt{(\omega_0)^2 - b^2/2} \tag{4}$$

at which the displacement amplitude A of the vibrating cantilever is the maximum value A_m.

According to the analysis shown above and including the effect of the mass of the cantilever, the fundamental natural frequency with no damping can be expressed as [8]

$$f_0 = \frac{1}{2\pi}\sqrt{\frac{3I_A E}{l^3}\left(\frac{1}{M + \frac{33m}{140}}\right)} \tag{5}$$

where E is Young's modulus of the material, I_A is the moment of area and is the function of the cross-section area of the beam, l is the effective length of the beam, M is the effective mass of the platform including loaded discrete mass and m is the effective mass of the beam.

This result applies for the case of a simple clamped beam with a mass added to the tip of the structure. The resonant frequency decreases in proportion to the inverse square root of the sum of the platform mass, added mass and a portion of the beam's effective mass. The device used for the experiment has two separated beams to support a platform. The plat-

form structure cannot be neglected, resulting in a more complicated deflection profile $Y(x)$. Analyzing this structure using analytical techniques is difficult and hence a computer aided finite element analysis was used.

2.1.3 Mass Sensitivity Simulation with ANSYS (see Appendix A for details)

ANSYS5.0 is a commercial finite element analysis package, which allows the simulation of mechanical properties (stress, natural frequency etc.), thermal transformation and couple field distribution. This package was used for simulation and analysis of the structure used for the mass determination.

The structural parameters used in the simulation were selected as following. The cantilever beams were 10 μm wide and 120 μm long, and the platform was 60 μm by 60 μm. The thickness was determined in terms of the thickness of dielectric layers in the CMOS technology. The material parameters were selected from reference [14].

To estimate the resonant characteristics of the sandwiched cantilever with and without loading, the modal analysis and the harmonic analysis were performed. A three dimensional finite element model with 736 nodes and 426 linear brick elements was used to model the cantilever in the modal analysis. The base of the cantilever beams were clamped in all degrees of freedom and 37 master nodes were selected for monitoring the motion of the cantilever. The fundamental mode shape is shown in Figure 3. The resonant frequency of the fundamental mode is 4697 Hz and this mode has a diving board motion with most of the curvature in the arms due to relative rigidity of the platform section. The tip of the cantilever has the maximum replacement in the fundamental mode. If a point

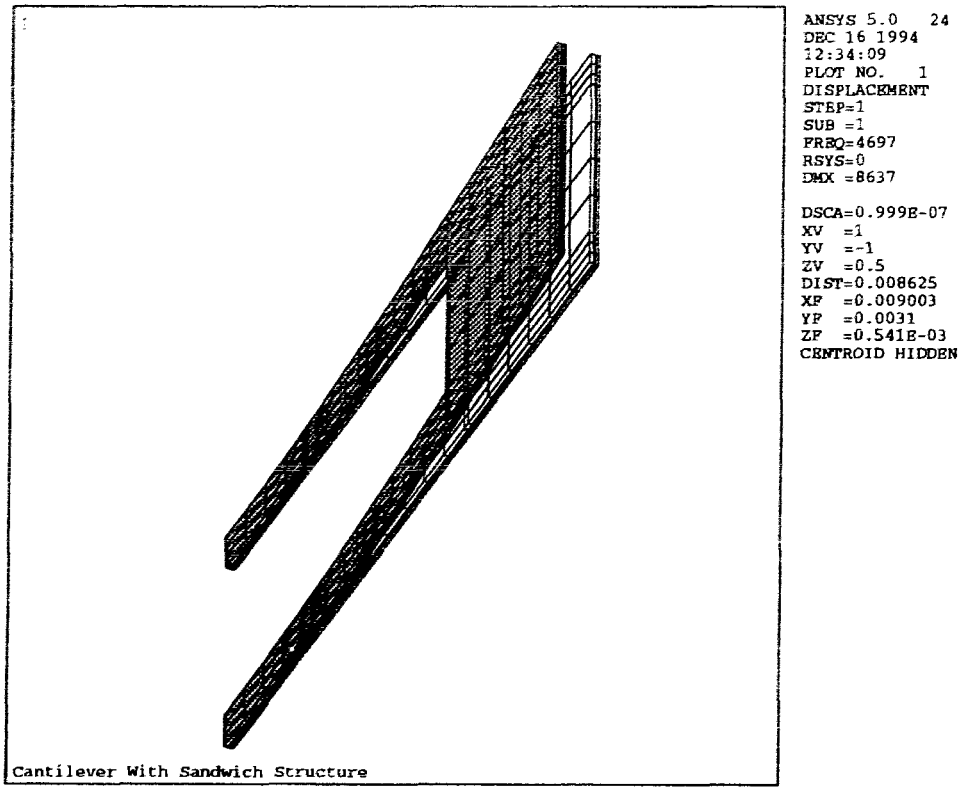

Figure 3: Fundamental mode shape

mass is placed at the tip of the cantilever, the maximum shift of the fundamental resonant frequency will occur [15]. For our analysis, a point mass was placed on the platform, 5 μm from the tip. The simulated resonant frequency shift in resource of loading for the fundamental mode is shown in Figure 4. The frequency shift versus loaded mass is almost linear at the range of less than 1.0 ng, and the slope is 149 Hz/ng at 0.1 ng loaded mass. According to equation (5), the square root function can be expanded into the series. If the added

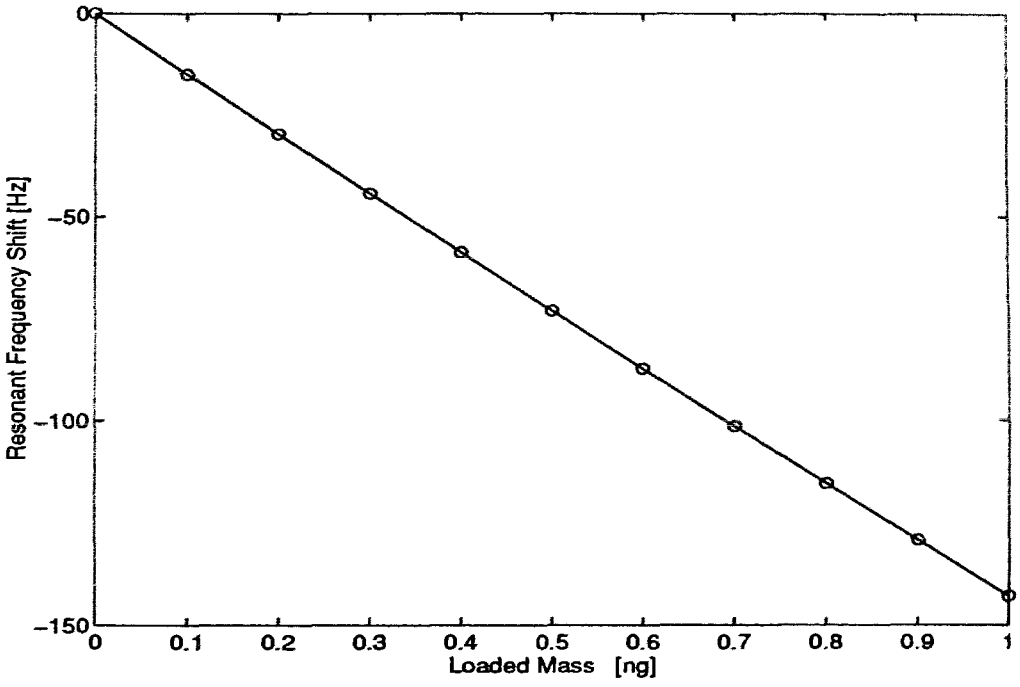

Figure 4: Simulated resonant frequency shift with loaded mass

mass causes very small effect on the effective mass of the platform (M), the first two terms of the series is a good approximation to the equation (5) and it shows a linear function. This agrees with the result of the ANSYS simulation.

With the harmonic analysis, we can get the resonant spectrum by monitoring the node's displacement. Figure 5 shows the spectra for loaded and unloaded devices. In the simulation, an experimentally determined damping factor of 0.03 was added to the model. The actuation was modeled by applying a periodic force on the tip with a value of 0.002 dynes.

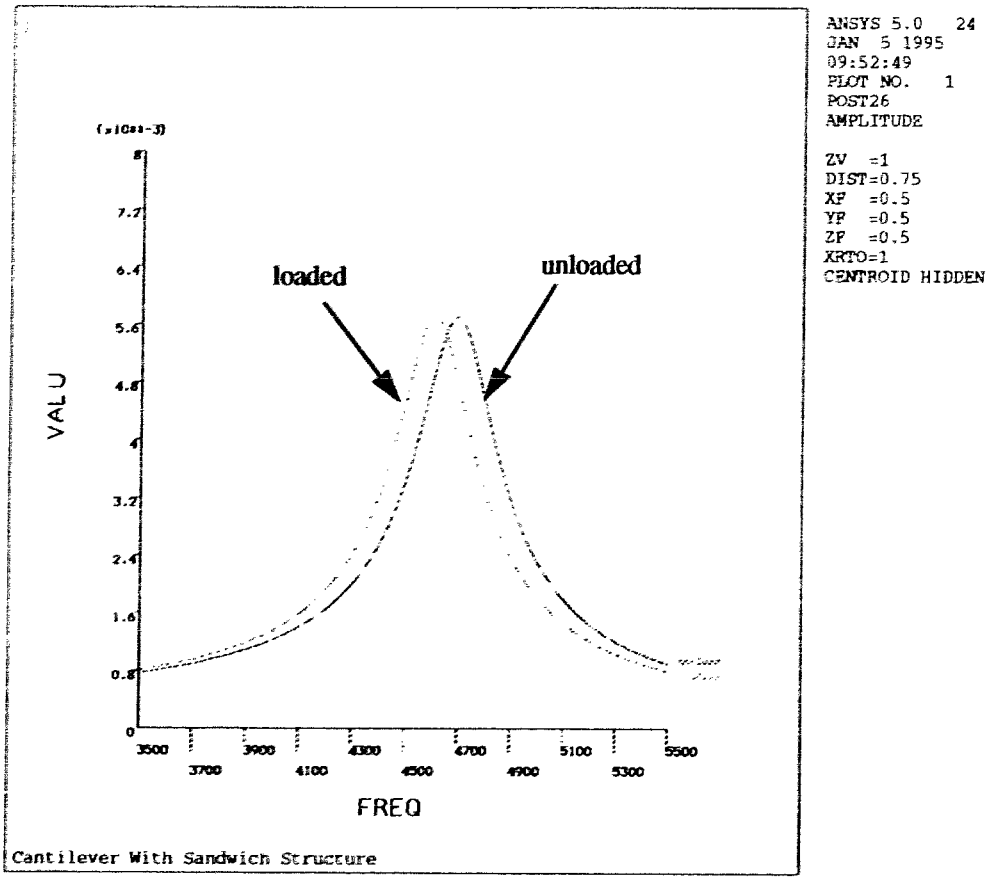

Figure 5: Simulated displacement amplitude spectra

The spectrum shows that the unloaded device is resonant at 4697 Hz, however, its resonant frequency is shifted to 4612 Hz with a 85 Hz shift when a mass of 0.586 ng is loaded. The results from the ANSYS simulation show that this device has an appropriate sensitivity in the sub-nanogram region.

2.2 Layout Design

CMOS-compatible micromachining technique involves the fabrication of certain micro-mechanical structures for sensor application on the CMOS chip. These micromechanical structures are fabricated by implementing unconventional layout designs in CMOS technology without altering the process sequence. A single post processing step (silicon etching) is introduced to form free standing micro-structures on CMOS IC chip without affecting the circuitry, thus allowing micromechanical sensors to be produced with on-chip circuitry for signal conditioning and processing. In general, fabrication of the circuitry is based on a given process sequence offered by a foundry. Any standard process is associated with pertinent layout design rules. Layout design rules affect only the mask but not the process sequence. Fabrication of free-standing sensor structure involves the patterning of the desired material layers available in CMOS technology and the selectively etching of the underlying support (silicon).

As is the case with all standard-process fabrication methods, design rules must be followed in order to obtain operational circuitry. These rules can somewhat be relaxed when designing sensor structures, as opposed to circuits on silicon. Circuit design rules are often broken in order to produce micromechanical devices. These violations appear only as design rule error flags but do not affect the circuitry.

2.2.1 Cantilever Layout Design

The cantilever layout design is shown in Figure 6. This consists of two support arm structure and a platform at the tip of the structure. The arm design is 10 μm wide and 120 μm long. The platform dimensions are 60 μm by 60 μm. The arm design also includes the gate

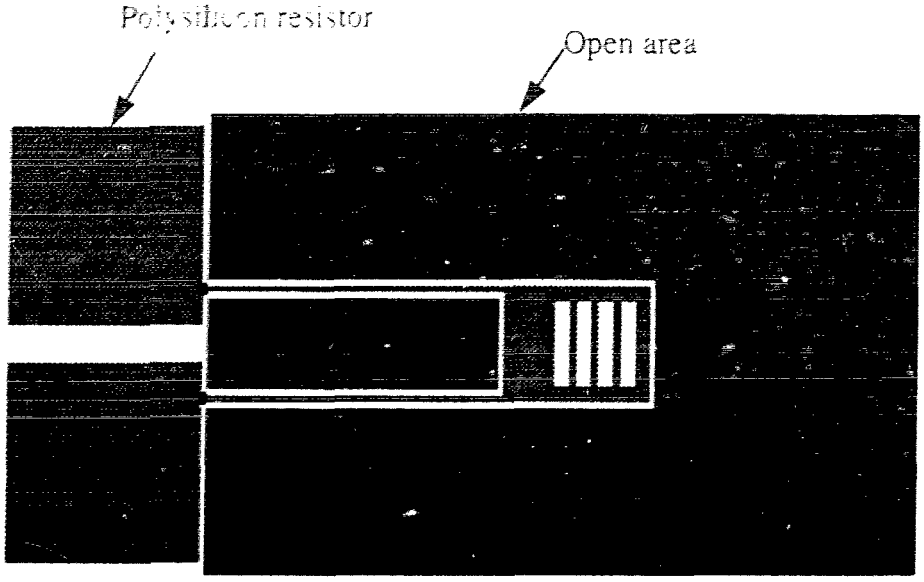

Figure 6: Layout of cantilever based on CMOS technology

polysilicon layer. An etch or opening layer is also defined (see Figure 6) which is mandatory for the CMOS compatible micromachining process to expose silicon. The opening layer consists of four layers (ACT, CON, VIA and PAS in MITEL 1.5 µm technology; CF, CC, CV and CG in NT CMOS3 technology) which are necessary to expose the substrate silicon.

Based on this layout design, the final structure will produce a composite structure formed out of the CVD oxide layers of CMOS process and the polysilicon. The polysilicon layers also forms a resistor, whose piezoresistance will be used for the detection of resonance of the structure. The polysilicon layer will be sandwiched between the CVD oxide layers, and hence, will not be destroyed by the anisotropic etchant during the postprocessing step. Further, the sandwiching oxide also prevents any liquid to come in contact with the poly-

silicon layer, allowing the possibility for exposing liquid ambient to the cantilever structure.

In order to make the electrical measurement simpler, three other polysilicon resistors were also integrated along side the cantilever structure, so that a Wheatstone bridge configuration can be arranged. This is illustrated in Figure 7.

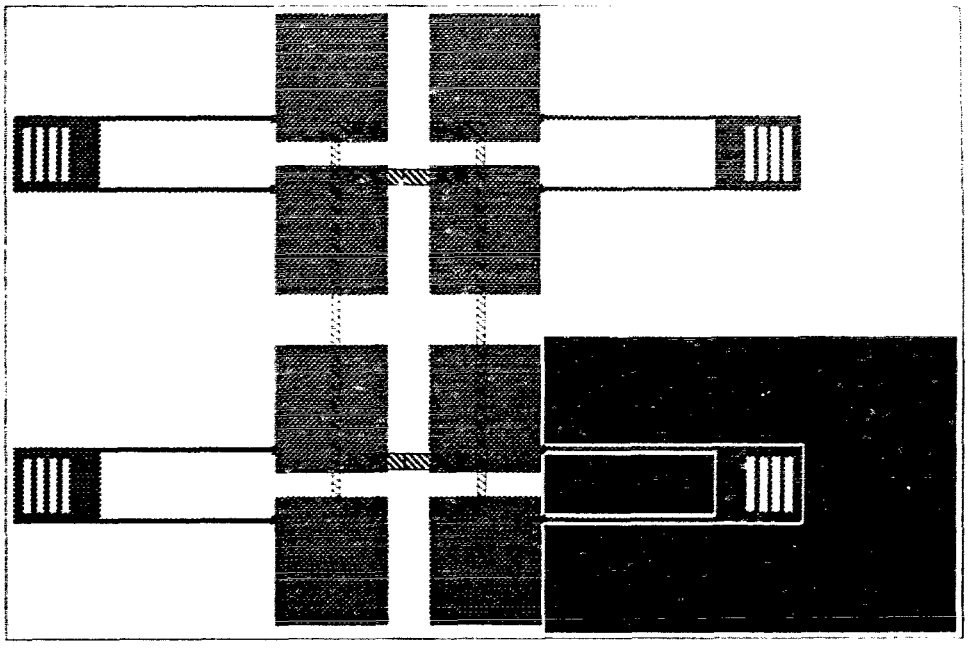

Figure 7: Layout of resistor bridge in CMOS chip

The four resistors are placed as close to each other as possible so that they can have same value. But they (except for the resistor sandwiched in cantilever) should be kept away from the etching cavity by at least 20 microns, therefore, the stress generated by etched cavity cannot affect the resistance.

2.2.2 On-chip Circuit Layout

In order to configure an integrated mass sensor system, an operational amplifier was also integrated along with the cantilever design. The schematic diagram of the circuit is shown in Figure 8. Transistors M1, M2 and resistor Rb form a current source. Transistors M3 and M4 are the differential input pair with M5 - M8 as active loads. M11 and M12 form the output stage. The output stage produces a DC level that is same as the input 2 so that the feedback resistor Rf does not affect the DC operating point. It also delivers a larger output current and offers a wider dynamic operating range. The circuit was simulated and optimized using HSPICE . The optimized W/L ratios of all the transistors, based on the Northern Telecom COMS 3 technology, are shown in the figure. Simulation indicates that the circuit has its open-loop voltage gain 85 dB.

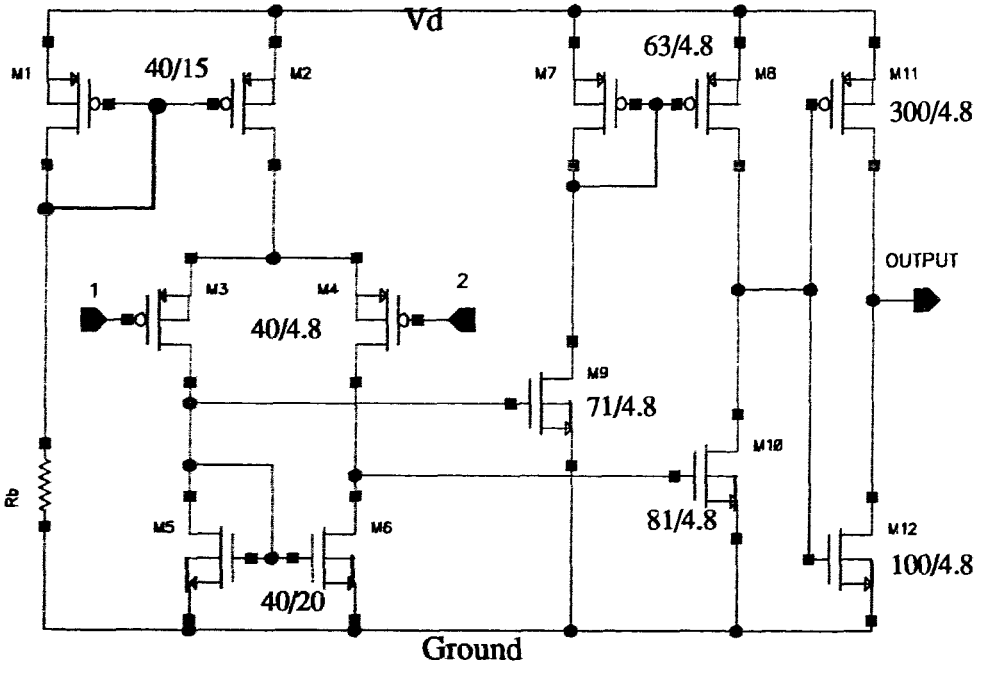

Figure 8: Schematic of the build-in operational amplifier in NT CMOS3

The bridge configuration formed by the four polysilicon resistors (one being the cantilever structure) was connected to the input of the circuit with a feed back resistor Rf. This is illustrated in Figure 9. Resistors R1 - R3 are the fixed resistors, and Rs is the sensor resistor. Any deformation of the cantilever structure will result in the resistance change because of the piezoresistance and this alters the balance of the bridge. If the cantilever is subjected to a periodic force, the output of the circuit will produce a periodic signal whose amplitude correspond to the amplitude of vibration of the cantilever structure. This output signal can then be processed for analysis.

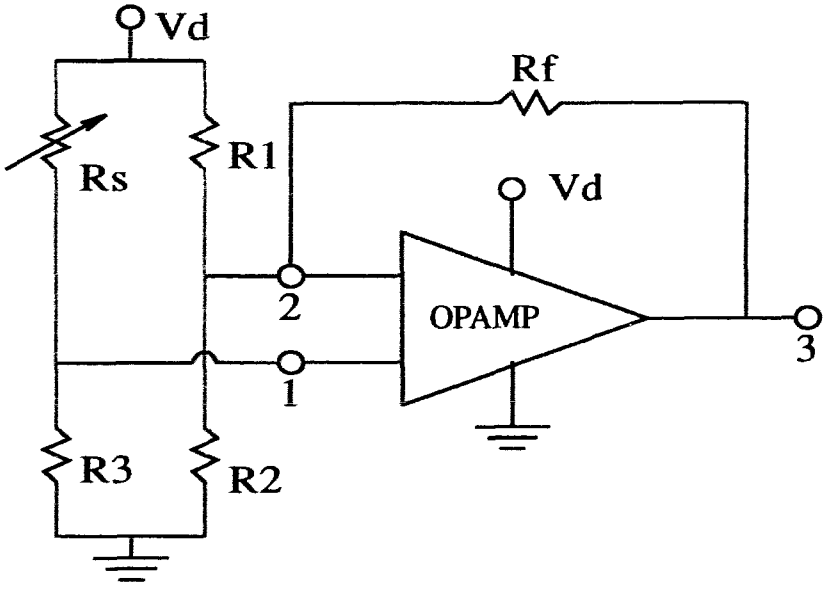

Figure 9: Block diagram of the integrated biomass sensor

Typical value of the polysilicon resistor is around 1.4 K. Using a feed back resistor value of 120 K, the closed loop gain of the amplifier becomes 44 dB.

Figure 10 shows the layout diagram of the circuit. The layout was generated for Northern

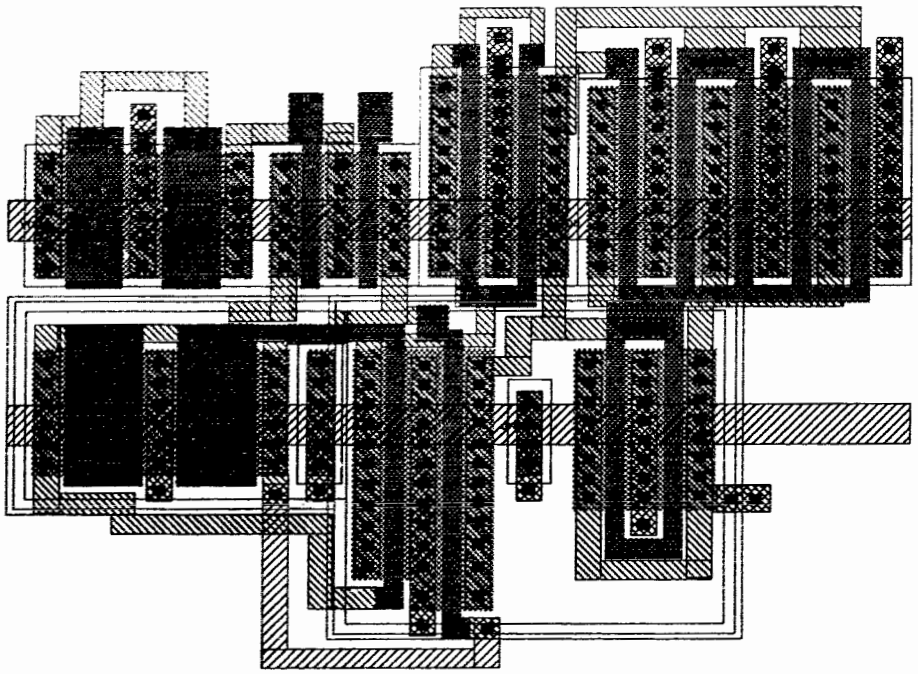

Figure 10: Layout of the operational amplifier in NT CMOS3

Telecom's CMOS 3 DLM process as well as MITEL's 1.5 μm Technology. The feed back resistor was not integrated along with the circuit, as it can be easily added to the circuit externally.

Chapter 3

Post-Processing of CMOS Devices

The layout designs were implemented on silicon by Northern Telecom electronics and Mitel Semiconductors (through Canadian Microelectronics Corporation). The devices were received in the form of chips and it required the micromachining step in order to form the cantilever structure. This was accomplished by the etching techniques outlined in the CMOS compatible micromachining process [5]. Since the etching process had to be performed on individual dies, a small glass holder for the chips was used to carry the dies inside the etching solution.

3.1 Anisotropic Etching

The chips were anisotropically etched using EthyleneDiamine Pyrocatechol in water (EDP). EDP offers an etch selectivity ratio between the {100} and {111} planes of 35:1. Also this etchant is quite suitable with CMOS processed chips because of no potassium or sodium contamination, and it does not attack the oxidation layer that seriously. The etch temperature was maintained at 95 ^{0}C and a cold water reflux arrangement was used in order to prevent the evaporation of EDP during the etching process. The etching apparatus is shown in Figure 11. The cross-section view of the etched silicon wafer is illustrated in Figure 12.

Typically an etch duration of 90 to 120 minutes were required to free all the cantilever structures on the chip. Periodic microscope inspections were performed in order to ensure

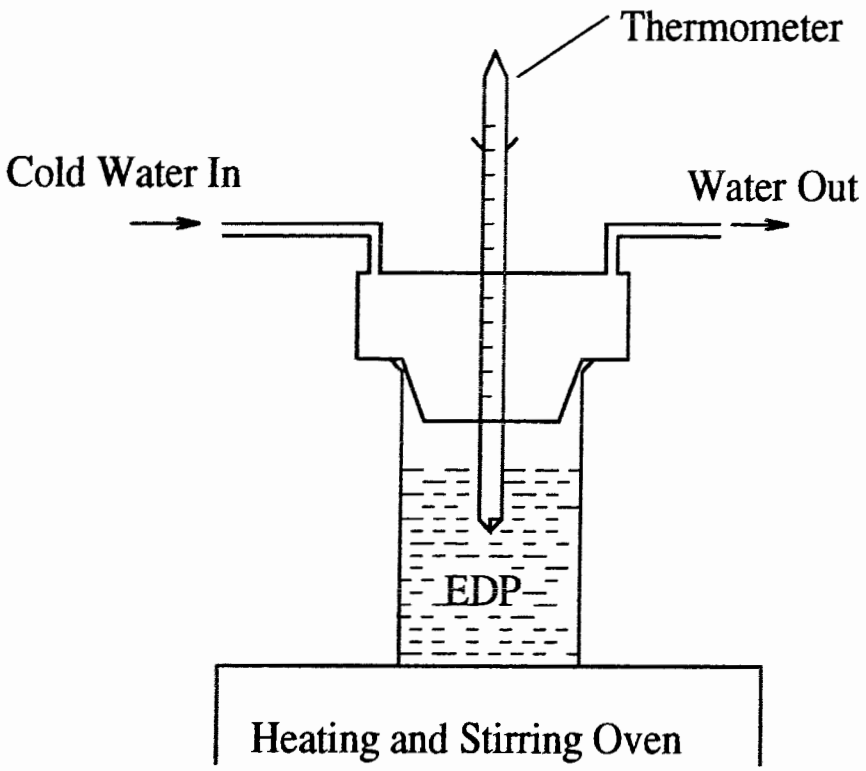

Figure 11: EDP etching apparatus

the correct release of the structure.

3.2 Cleaning

Any etching process leaves considerable residue on the surface and requires thorough cleaning. After the EDP etching step the devices (along with the holder) were transferred quickly to a beaker containing hot DI water at 90 ^{0}C. The chips were allowed to rinse in this condition for 10 minutes and then were transferred to another beaker at 50^{0}C DI water. After this step, the devices were transferred to room temperature DI water rinse and

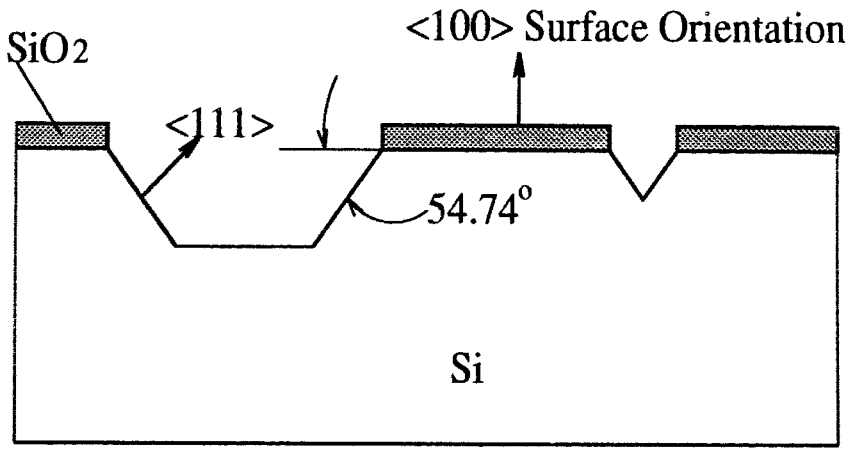

Figure 12: Cross-section of the etched cavity shape

cleaned for 20 minutes. Finally the devices were individually removed from the water bath and rinsed with acetone and allowed to dry naturally.

3.3 Bonding Pad Protection

If CMOS chips were exposed to EDP for a duration longer than 30 minutes, most of the times the aluminum bonding pads are attacked by EDP. If electrical connection is required to microstructure then the bonding pads should be protected.

3.3.1 Electroless Nickel Plating

Electroless plating of nickel can be used to protect the bonding pads against the attack

from EDP. This can be accomplished by the process described in [16]. First the exposed aluminum pads should be zincated and a layer of nickel is deposited using electroless plating technique. Subsequent to this a thin layer of gold can be coated on top of the nickel surface by electroless gold coating. This process should be performed on the CMOS chips prior to post-processing.

3.3.2 Special Pad Design

One other technique to protect the bonding pads is to make a special design for the bonding pads. Usually the bonding pads designs are made using both the metal layers available in the CMOS process with the inter-metal dielectric isolation removed. This has to be designed by the user by using the VIA layer. The design can be altered such a way the inter-metal dielectric can be left between the two metal layers of the bonding pad. During the anisotropic etching only the top metal layer is attacked and the bottom metal layer will be protected by the dielectric. This leaves the aluminum pads below the dielectric with sufficient area for bonding. To bond to this aluminum the bonding machine has to break through the dielectric layer. Hence, a slightly higher power should be applied to the bonder-tip in order to break through the dielectric layer.

This approach has given sufficiently good result and many devices were bonded and used for the experiment.

3.4 Other Etchants for CMOS-Compatible Micromachining

Hydrazine is another anisotropic etchant for silicon. It does not affect the aluminum pad and has longer life time and there is no residue. However, this etchant poses severe safety hazards due to its explosive nature. Further, its anisotropy ratio is much lower, and there will be a large lateral etching and undercutting. Consequently this introduces difficulty in the layout design.

TMAH (Tetramethylammonium Hydroxide) can be also used for anisotropic silicon etch. We found the etching rate is lower than EDP in our laboratory experiments. This etchant also attacks aluminum and exhibits large lateral etching.

Chapter 4

Piezoresistance of CMOS Polysilicon

Polycrystalline silicon has been shown to be a suitable strain gauge material [9] with its high gauge factor compared with metal film sensors, but lower than single-crystal silicon. The gauge factor is defined as the fractional change in resistance per unit strain [9]:

$$G = \frac{\Delta R}{R\zeta} \tag{6}$$

where ζ is the applied strain, R is the resistance and ΔR is the resistance change due to the applied strain.

The gauge factor is an important parameter to describe the piezoresistive property of a material. The result of the theoretical analysis shows that the gauge factor of the polysilicon film is the function of the grain size and the doping concentration. The details are shown in Appendix B. The experimental results of CMOS gate polysilicon are shown in this chapter.

In CMOS technology, the polysilicon gate material is deposited with LPCVD (Low Pressure Chemical Vapor Deposition) method at a temperature between 620 to 640 °C. The reaction gas is silane (SiH4). The surface of the substrate is heated to create the decompo-

sition of silane into silicon and hydrogen in accordance with the following reaction:

$$SiH_4 \xrightarrow{T} Si + 2H_2$$

The conditions of this reaction determine the deposition rate and structure of the films. Contributing factors are the mass transport rate and the surface reaction rate of the SiH_4 molecules on the film surface. A reduction of the pressure will lead to an increase in the mass transport rate, since the diffusion rate is inversely proportional to the total system pressure ($D_n \propto 1/P$). Therefore, in LPCVD processes the deposition rate is determined by the surface reaction rate. This reaction will depend mainly on the deposition temperature and on the partial pressure of the reaction gas. The temperature will also determine the structure of the deposited film. Typically, below 585 °C the material deposited is amorphous, above 600 °C it is polycrystalline, with an average grain size increasing with increasing deposition temperature. Doping of the polysilicon film can be carried out by one of the following three procedures: (1) by addition of a doping gas such as diborane or phosphine into the reaction gas mixture; (2) by diffusion; or (3) by ion implantation. In CMOS process, the very high dopant concentration in gate polysilicon is expected in order to obtain good conductivity. Uniformity and repeatability of the doping process are important as well. The doping of polysilicon films is thus done primarily by ion implantation.

In the experiments, two types of CMOS chips were fabricated by two different manufacturers. One is from Northern Telecom (NT CMOS3), and the other is from MITEL (MITEL CMOS1.5). For NT CMOS3 chip, the polysilicon resistor sandwiched in the cantilever was deposited on the field oxide layer (7500 Å) with LPCVD at the temperature 620 °C. The thickness of the polysilicon film was 3500 Å. The doping was performed by phosphorus ion implantation. Then the polysilicon is patterned. After that, the CVD SiO_2 layers are deposited, followed by the passivation layer deposition. The resulting CMOS

chips were post-processed in our laboratory. The cantilever was released with EDP as the silicon anisotropic etchant.

The piezoresistance of the polysilicon resistor sandwiched in the cantilever were investigated experimentally. The bonded chip was mounted on a connection board, and it was firmly fixed under a microscope. The polysilicon resistor was electrically connected for measurement. A probe was used to push the cantilever down in order to introduce a stress in the cantilever beam. The probe tip was placed on the platform portion of the cantilever. Using an adjustable screw, the cantilever was bent down. The displacement of the cantilever tip was determined using the focus of the microscope. The reading error was estimated to be about one micron. The experimental data is shown in Tables 1 and 2.

Table 1: Piezoresistive Properties of MITEL CMOS Polysilicon

Δx (μm)	0	7	15	23	35	43
r_1 (Ω)	1152	1164	1180.5	1193	1215	1238
Δr_1 (Ω)	0	12	27.5	41	63	86
σ_x (10^5 dyne/cm^2)	0	2276	4877	7478	11380	13980

Table 2: Piezoresistive Properties of NT CMOS Polysilicon

Δx (μm)	0	16	32	56	83
r_1 (Ω)	1456.5	1488.5	1524	1600	1691
Δr_1 (Ω)	0	32	67.5	143.5	234.5
σ_x (10^5 dyne/cm^2)	0	5202	10400	18210	26980

In the tables Δx is the displacement of the cantilever tip (difference between the focus positions), r_1 is the resistance of the polysilicon resistor, which changes with the displacement of the cantilever tip, Δr_1 is the change in resistance r_1 for the respective displacement of the cantilever tip, and σ_x is the stress, which is obtained from simulation with ANSYS. When the tip of the cantilever has a certain displacement, there is a distribution of the stress along the cantilever beam. With the static structure analysis using ANSYS, we can obtain the stress distribution. The cantilever beam was 120 μm long and 10 μm wide and the polysilicon resistor was relatively thin and was covered by silicon dioxide layers so that the beam can be considered as a isotropic thin wire. Thus the stress and strain relation can be simply expressed as $E = \frac{\text{stress}}{\text{strain}}$, where E is Young's modulus. Based on this, the strain distribution can be estimated. It should be noticed that the cantilever consists of a several layers of silicon dioxide and a polysilicon resistor. Since the cross-section area of the polysilicon resistor is much smaller than that of SiO_2 layers (less than 1:10), the SiO_2's Young's modulus can be used in the calculation instead of silicon's Young's modulus as a close approximation

Figure 13 and 14 show the change and relative change ($\Delta r_1/r_1(0)$) in resistance of the polysilicon versus the displacement of the cantilever tip, respectively. Using these figures, we can compare the results from the chips manufactured by MITEL and NT. For MITEL

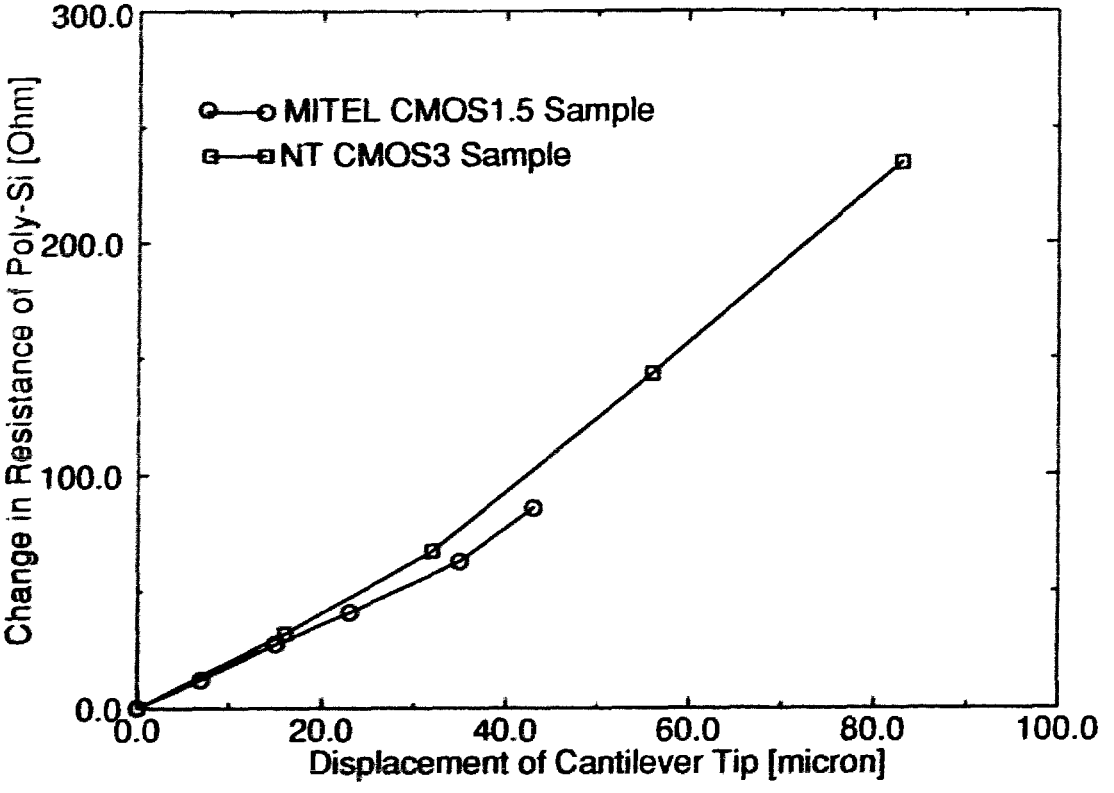

Figure 13: Resistance change vs. displacement of cantilever tip

chip, the change in resistance is slightly smaller than that of NT chip, but the relative change in resistance is slightly larger than that of NT chip. For example, at the displacement of around 15 μm, the change and relative change in the resistance of MITEL chip are 27.5 ohms and 2.4% respectively, but for NT chip, they are 32 Ohms and 2.2% respectively. Another thing we can observe is that when the displacement of the cantilever is smaller the resistance changes linearly with the displacement, and when the cantilever tip is bent downward more than 35 μm, the resistance change deviates from the linearity. This

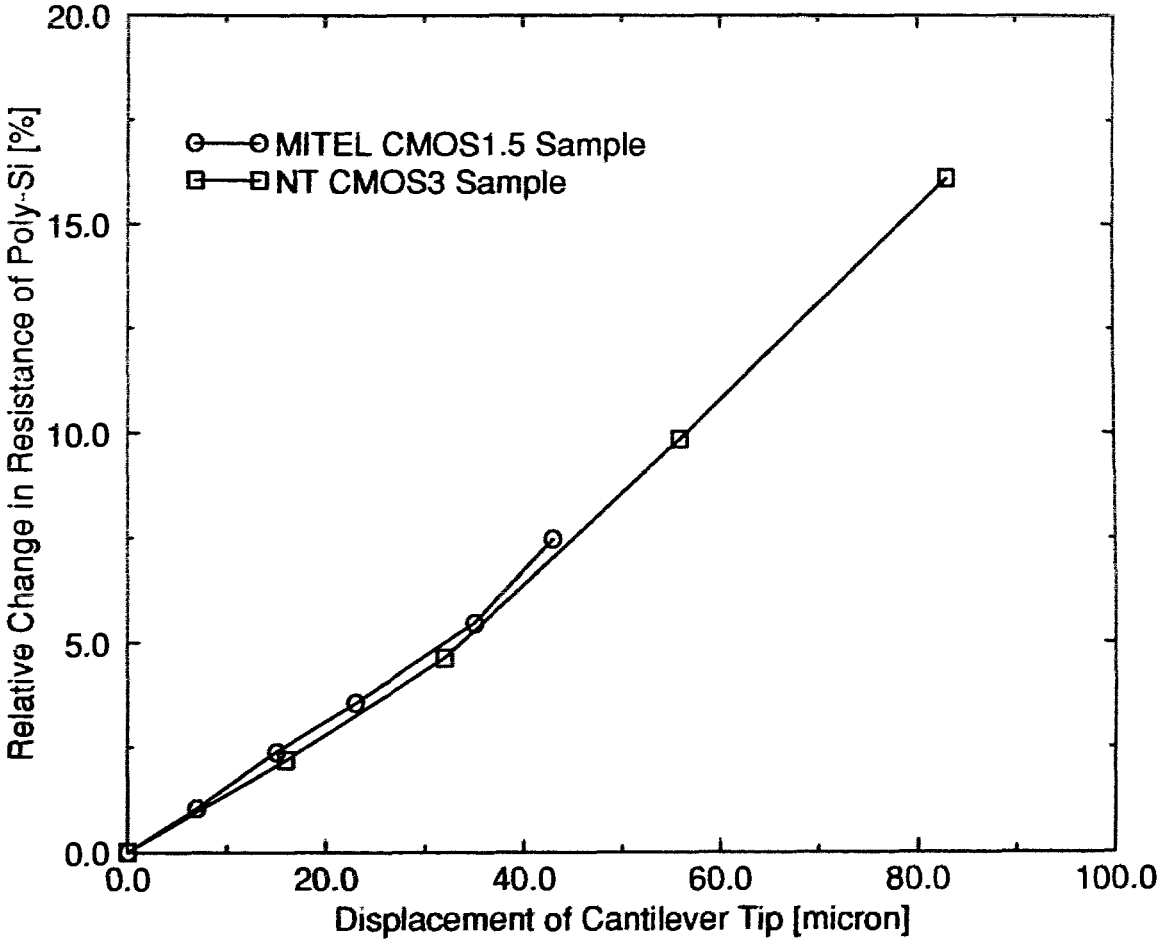

Figure 14: Relative change in resistance vs. displacement of cantilever tip

feature of the gate polysilicon material is good for the resonant sensor, as near the resonant frequency, the cantilever vibrates at the largest amplitude. Thus maximum resistance change can be obtained for measurement.

The resistance of the gate polysilicon as a function of the strain introduced in the cantilever is shown in Figure 15. It shows that the resistance of the gate polysilicon material on both chip is the linear function of the strain when the strain is smaller. In the experiments,

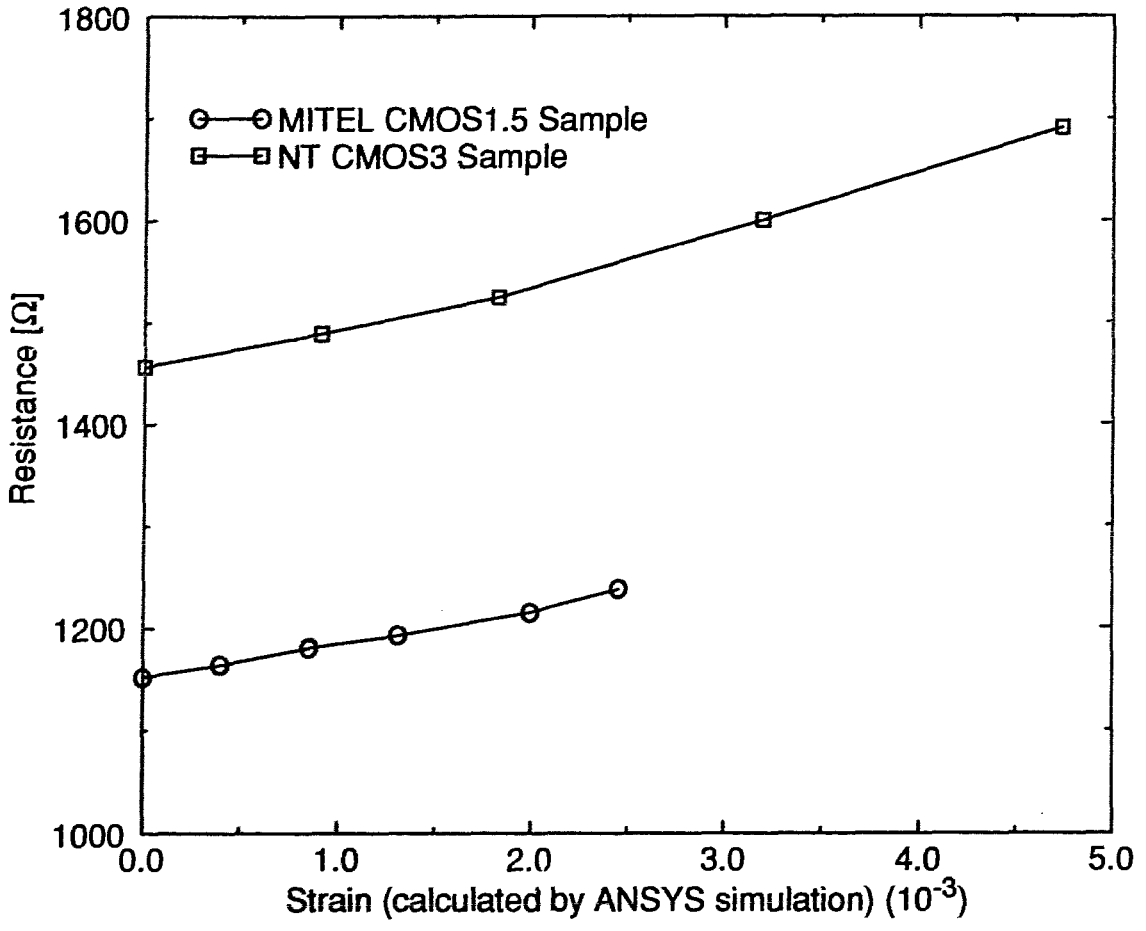

Figure 15: Resistance as a function of strain

the change in resistance for increasing and decreasing strain were the same. When the probe is pushed down and released, the resistance will totally recover back to the original value. It can be shown that when the cantilever is pushed down the sandwiched polysilicon resistor experiences a compressive strain, thus the resistance of n-polysilicon gate material increases. In MITEL CMOS1.5 technology, the cantilever consists of (from bottom to top) field oxide 9000 ± 500 Å, polysilicon gate 3225 ± 300 Å, dielectric layer SOG/

PSG/SOG 1300/5000/1800 Å, inter-metal-dielectric-1 3000 ± 300 Å, spin-on-glass 4200 Å, inter-metal-dielectric-2 3000 ± 300 Å and finally passivation: oxide/nitride 5000/5000 Å. We can see that there is about 2.8 μm thick dielectric layer above the polysilicon, but only 0.9 μm thick dielectric layer below it. When the cantilever is bent down, the top part of it experiences tensile strain but the bottom part experiences compressive strain, so that the polysilicon experiences an effective compressive strain and consequently the n-polysilicon resistance increases. This was confirmed by the fact that the resistance of the polysilicon in the cantilever beam decreased from 1168 Ω to 1152 Ω after etching cavity. The cantilever was observed to bend upward by 8 μm after releasing. As the cantilever bends up, the polysilicon is experiencing tensile strain and the resistance decreases. Also, it was confirmed using ANSYS simulation.

The gauge factor defined by equation (6) can be obtained in terms of the experimental data. For the samples from MITEL CMOS technology, the gauge factor is 25, and the relative resistance change $\Delta r_1 / r_1(0)$ at the displacement of 15 μm is 2.4%. The samples from NT CMOS3 have the gauge factor of 24 and the relative resistance change of 2.2% at the displacement of 16 μm. Thus, we can conclude that the gate polysilicon in NT and MITEL CMOS technology has a good gauge factor. This also compares well with the results in [9], and it can offer the advantage of potentially higher operating temperature limit than diffused single-crystal silicon strain gauge devices. The most interesting advantage is that the good piezoresistance of gate polysilicon material in CMOS technology can increase the scope of CMOS-compatible micromachining technology and can be applied to more sophisticated and intelligent transducer systems.

Chapter 5

Experimental Set-up

In order to experiment the sub-nanogram measurement system, the following experimental set-up, shown in Figure 16, was used. The principle behind the testing was to excite the cantilever structure using a sweeping sinusoidal signal and detect the oscillation amplitude of the cantilever synchronously using a signal analyzer.

A miniature vibration table, MINI SHAKER TYPE 4810, was used to excite the cantilever. A SR850 lock-in amplifier was used to generate the sweeping sinusoidal signal as well as the signal detection system. The sine output was fed to an amplifier (PR7220 25W) which in turn drives the vibration table.

The piezoresistor terminals were connected to a DC voltage source and hence when the resistance changes a time varying current signal develops through the terminals. The polysilicon resistor in the cantilever forms one of the bridge resistors. A DC voltage is applied to the bridge so that the resistance changing will result in bridge imbalance. This signal is fed as input to the lock-in amplifier. This signal spectrum can be displayed on the screen of RS850, as well as stored in the memory. The displayed or stored points of the spectrum can be a maximum of 64 K. If the driving signal is sweeping from 1Hz to 64 KHZ, the interval between two points (reading resolution) is 1 Hz, and 0.1 Hz reading resolution can be obtained if the sweeping is from 1 Hz to 6.4 KHz. So the reading resolution can be fairly accurate without compromising the sensitivity. The peak of the oscillation spectrum, which is the resonant frequency point, can be read on the screen. The recorded data can be directly sent to a computer for analysis.

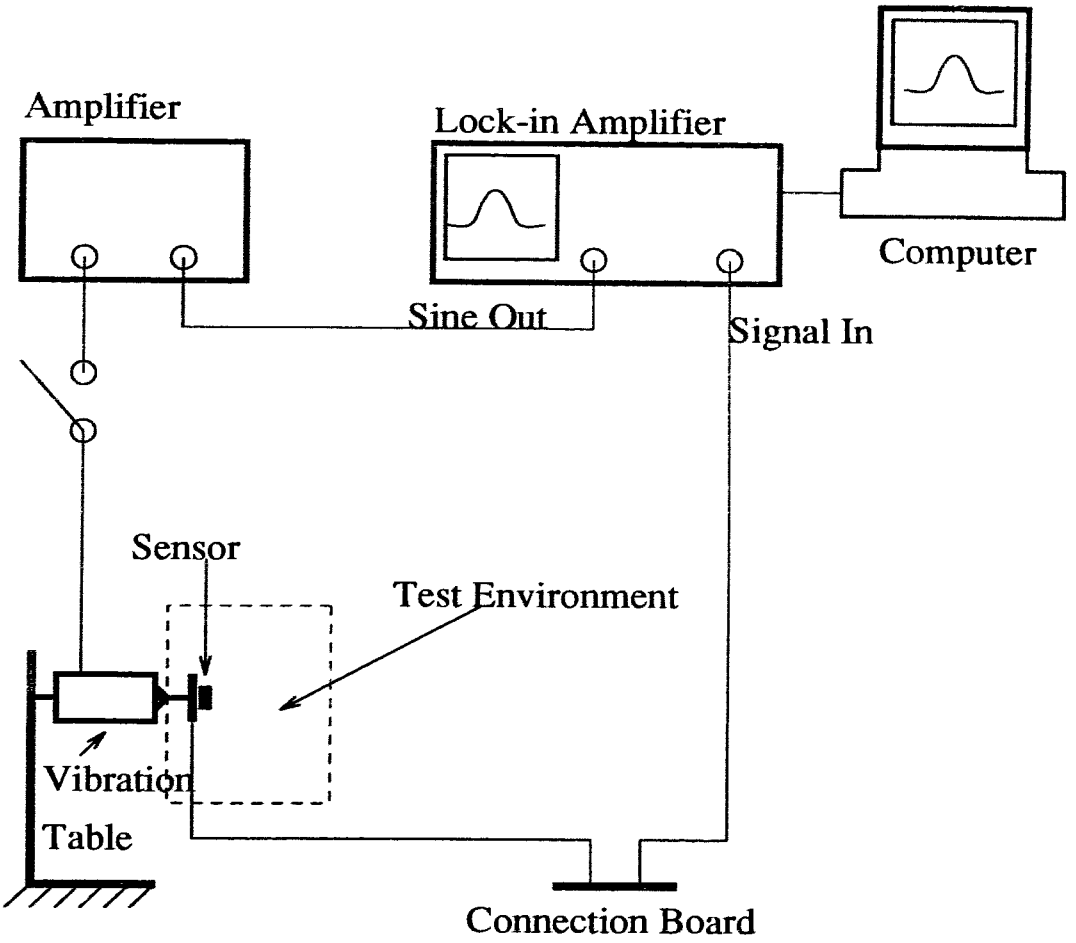

Figure 16: Measurement set-up

Chapter 6

Results and Discussion

CMOS chips (MITEL CMOS1.5 chip and NT CMOS3 chip) were etched by EDP at temperature of 95 °C for 120 minutes. The average depth of the etched cavity was measured to be 110 μm. Figure 17 shows the unetched and etched cantilever structure. The dimen-

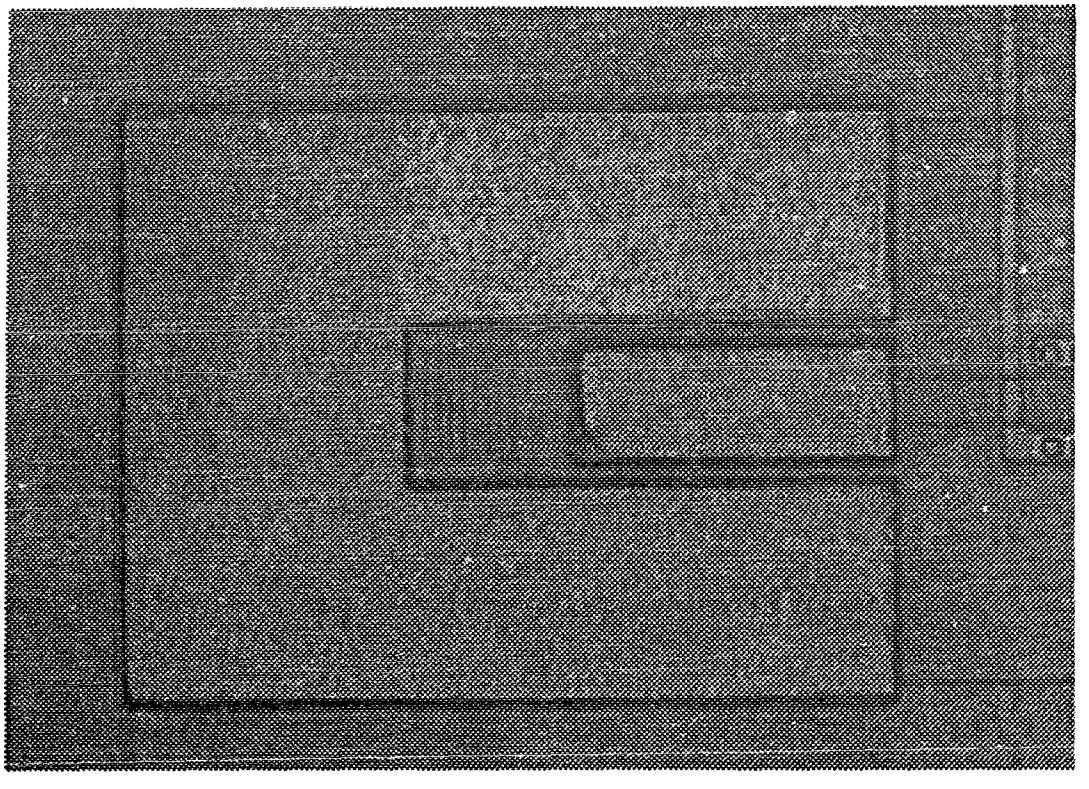

Figure 17 (a): Cantilever structure before postprocessing

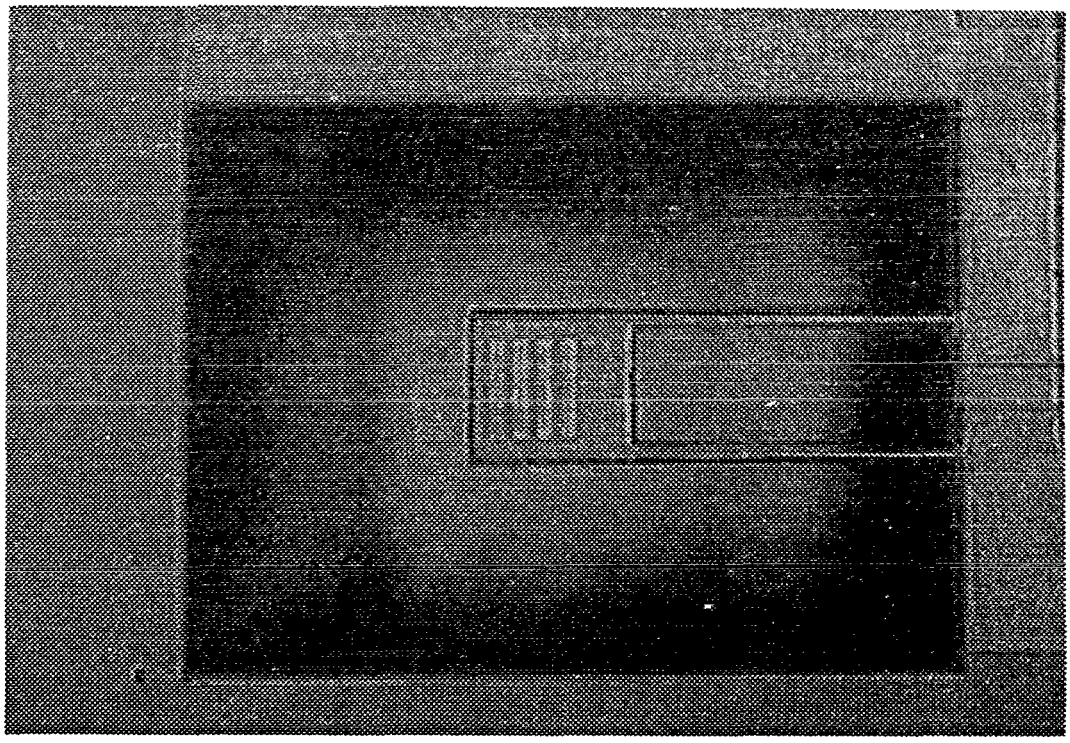

Figure 17 (b): Cantilever structure after postprocessing

sions of the released cantilever was checked under the microscope. The width of the cantilever beam was 9.8 μm, compared with the design value of 10 μm.

Figures 18 and 19 are the photomicrographs of the on-chip circuit before EDP etching and after EDP etching. We can see the circuit area did not show any visible damage due to post processing. The electrical characteristics of the circuit also remained the same after post processing.

Figure 20 shows the microphotograph of the four polysilicon resistors including the canti-

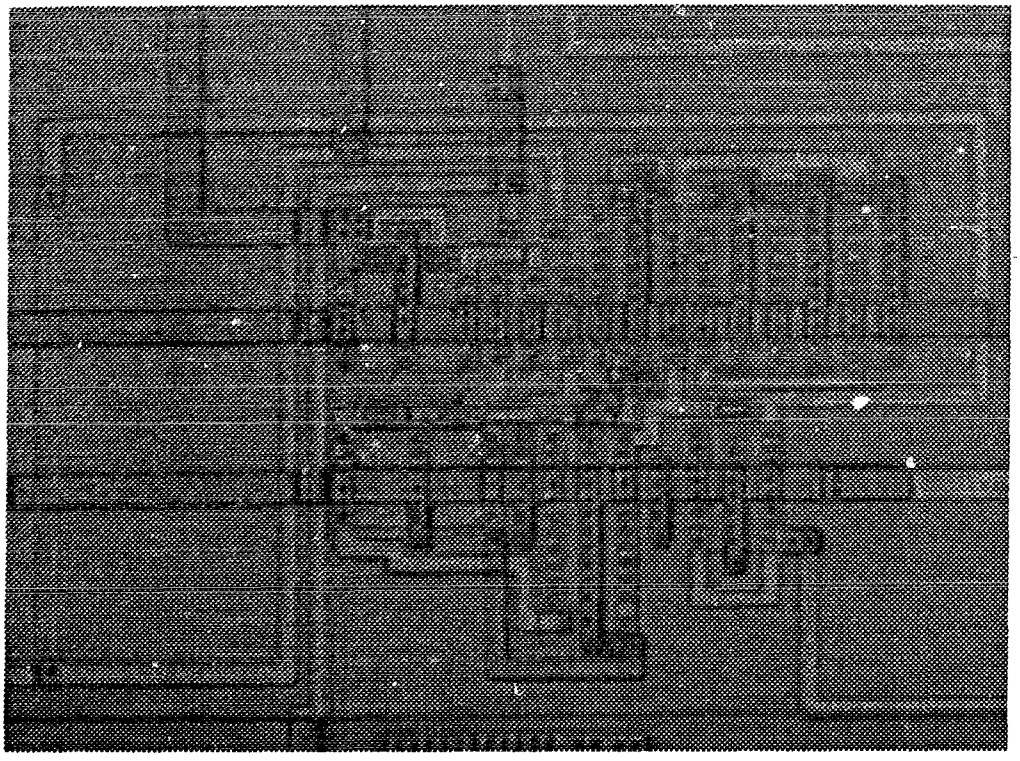

Figure 18: On-chip circuit before postprocessing

lever and amplifier. Four polysilicon resistors combine of a Wheatstone bridge. One pair of terminals were connected to a DC bias and the other two were connected to two differential inputs of the amplifier. When the free-standing cantilever vibrates, the resistance of the polysilicon sandwiched in the cantilever will change because of the piezoresistivity, and the bridge will output an AC signal. This signal can be amplified and detected.

Calibration measurements were performed using polystyrene calibration spheres obtained from Duke Scientific Corp. These spheres have a well defined diameter and density and thus a known mass The polystyrene sphere used for this experiment has the diameter of

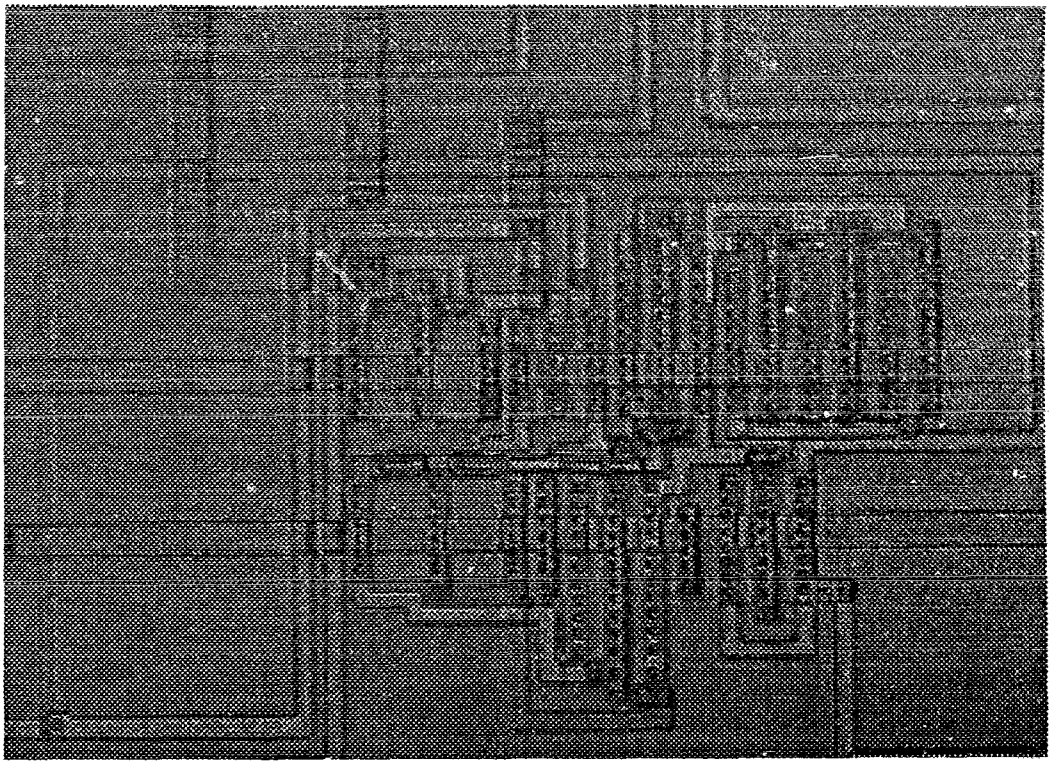

Figure 19: On-chip circuit after postprocessing

10.2 µm and a mass of 0.586 ng. Figure 21 (a) and (b) shows the cantilever with one and two polystyrene spheres loaded, respectively.

6.1 Measurement

The measurement set-up is illustrated in Figure 16. The Lock-in Amplifier receives the electrical signal from the resonant sensor with the same frequency as the driving signal. The oscillation spectrum can be displayed on the screen of the lock-in amplifier and can be

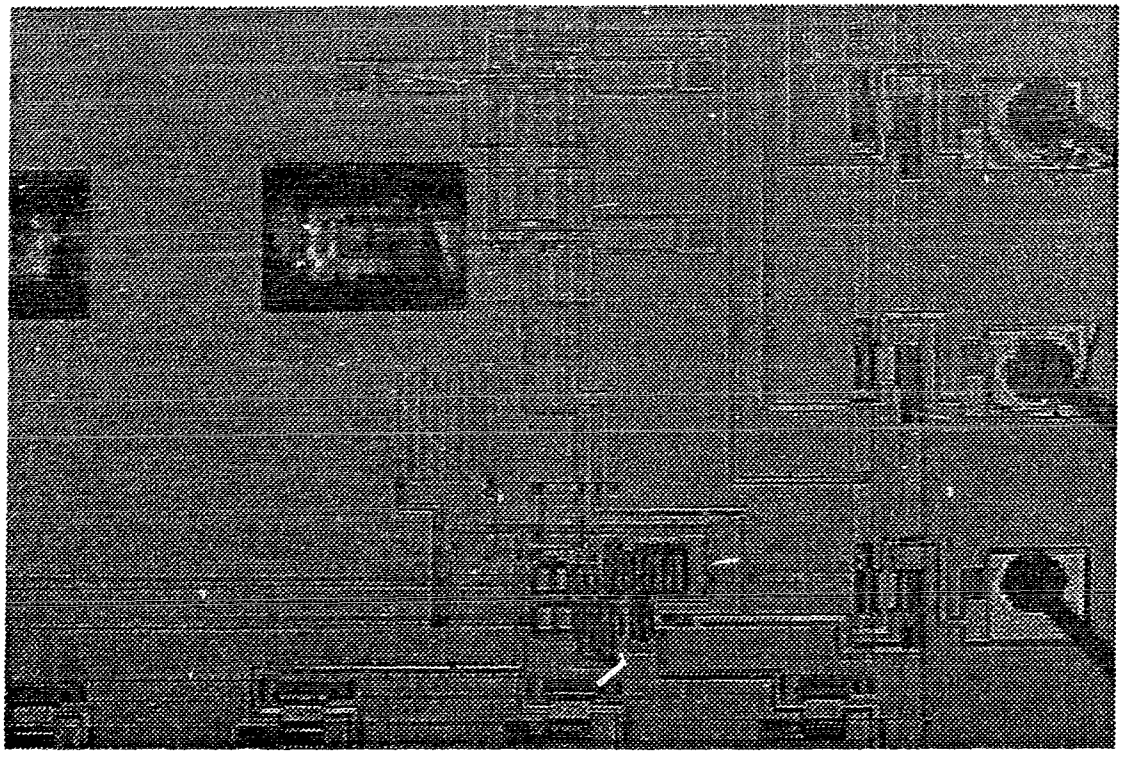

Figure 20: Photomicrograph of the integrated device

saved as two data formats on a disk. One is the machine data file, which includes the data in the active display trace and the instrument state. It can be recalled on the screen of the lock-in amplifier. The other data format is ASCII data file which may not be recalled by the lock-in amplifier, but it can be conveniently transferred to the computer for analysis. The resonant frequency (the peak of the oscillation spectrum) can be read on the screen of the lock-in amplifier or using the computer. Figure 22 shows the typical oscillation spectrum resulted from the measurements. This device has a resonant frequency of 3.806 KHz.

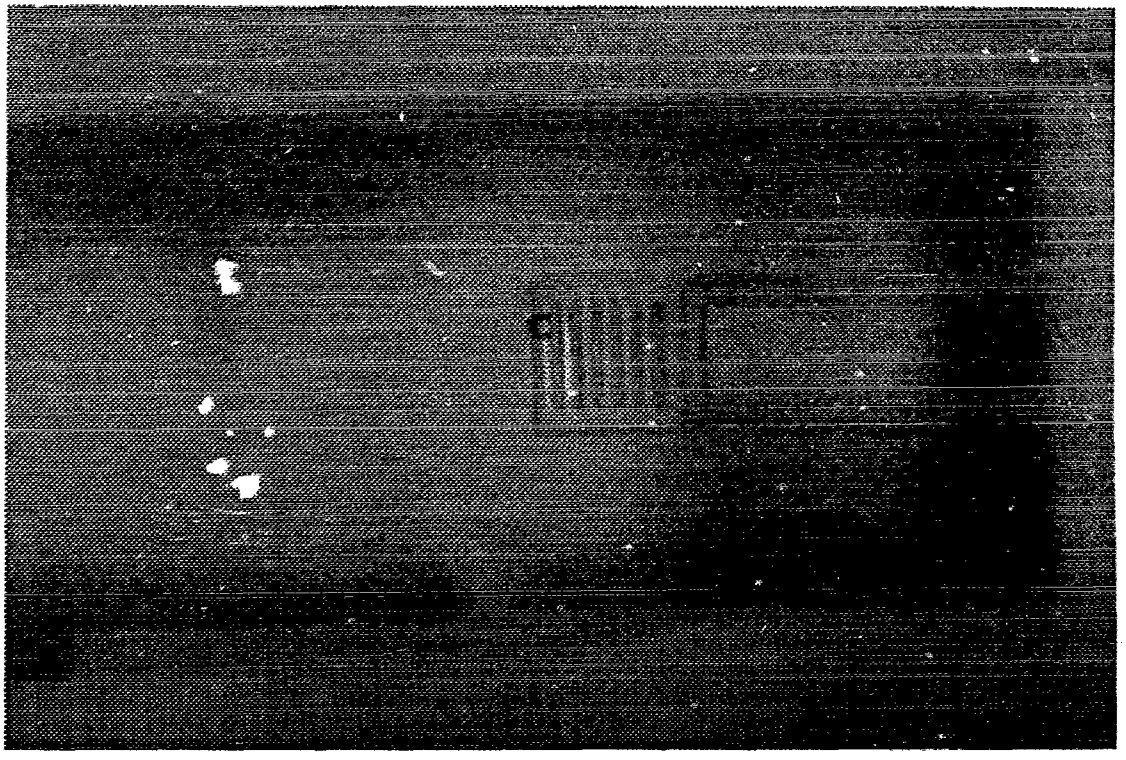

Figure 21(a): Cantilever with one loaded polystyrene sphere for calibration

6.1.1 Quality Factor

The quality factor of a resonant sensor is very important parameter for resonant devices. It is defined as the ratio of the resonant frequency to the bandwidth at 0.707 of the maximum amplitude (or half power), expressed with a formula as

$$Q_F = \frac{F_0}{\Delta F} \tag{7}$$

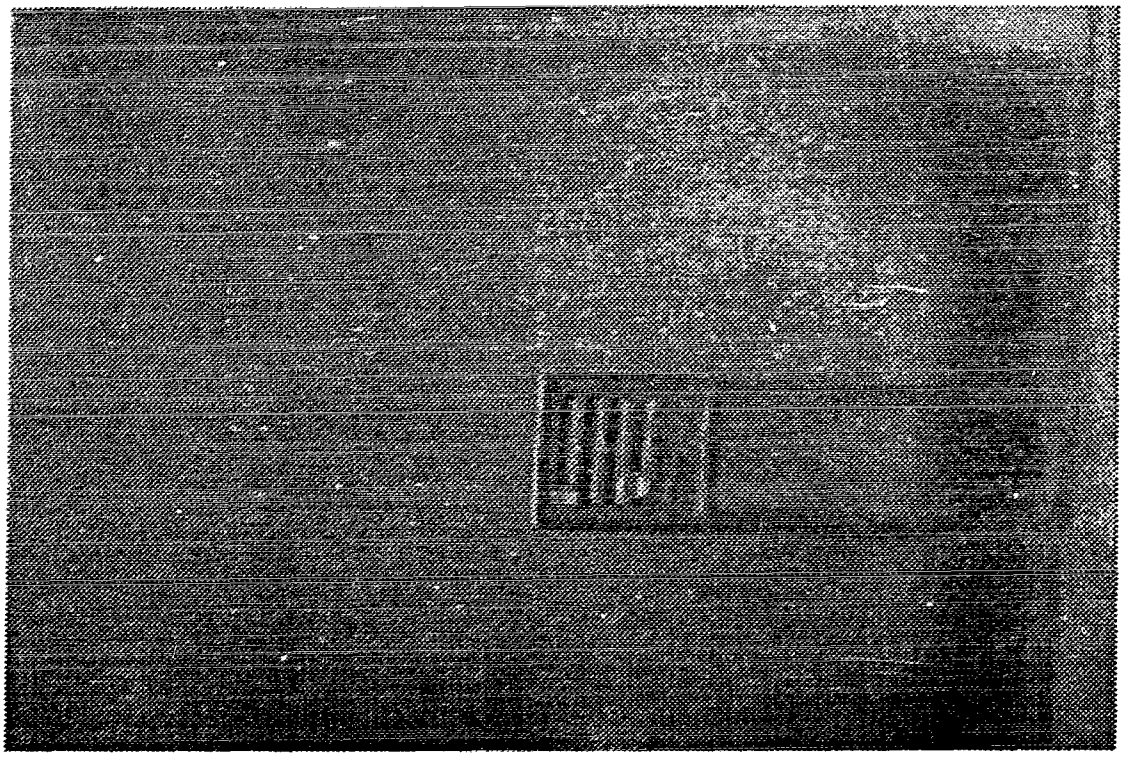

Figure 21(b): Cantilever with two loaded polystyrene spheres for calibration

where F_0 is the resonant frequency and ΔF is the bandwidth of the spectrum at 0.707 of the maximum amplitude. The quality factor of a resonant sensor is directly related to the sensitivity. The higher the quality factor, the higher the sensitivity. This is because a smaller shift in resonant frequency can be resolved when the device exhibits high quality factor.

The Q factor is related to the damping of the system also. Increased damping reduces the

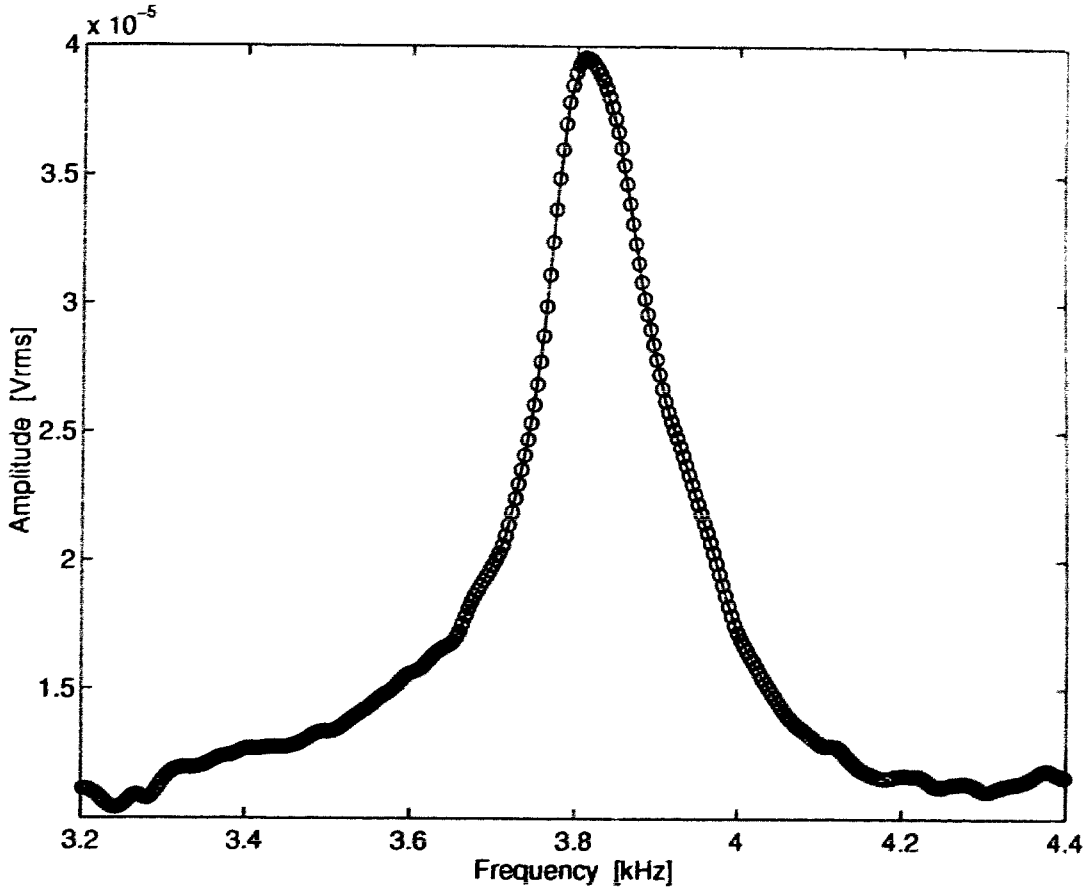

Figure 22: Measured oscillation spectrum

Q, making resonances less sharp and resonant amplitudes smaller for a given actuation. When the Q is reduced to 0.5, the device is said to be critically damped [17] and the device will not oscillate or resonate. The two types of damping contributing to the Q factor are structural and viscous.

Structural damping is the dissipation of energy when materials are cyclically stressed. And it is a result of material parameters and device configuration. The structural damping is

independent of frequency and proportional to the square of the amplitude of vibration. For a resonant system, structural damping can be minimized by selecting a device configuration so that the device is more flexible. For torsional resonance, the torsional member should be made relatively thin. For angular resonance, the flexing member should be thin and any supports which resist this flexing motion should be minimized or eliminated.

Drag between a moving body and its surrounding medium causes viscous damping. Increased viscosity of the medium corresponds to more drag and therefore more viscous damping. If the medium is very viscous and the device produces significant drag, resonance cannot be achieved. Viscous damping can be minimized by operating in inviscid medium such as air or eliminated by operating in a vacuum. But for many discrete mass measurement applications, such as the case in this thesis work, operation in a viscous fluid will be required. The viscous damping can be reduced by reducing the drag produced by the body. Drag can be reduced by reducing the frontal area pushed through the fluid. The cantilever structure used in our project has two beams and a pay-load platform, which is necessary for loading discrete masses. This structure has a minimized frontal area and the two beams depress the lateral and torsional vibration. Combining with the piezoresistivity, this cantilever structure has a better quality factor. The measured data indicates that it has a quality factor of 41 in air and 22 in DI water.

6.1.2 Sweeping Time Effect

In the measurement set-up, the vibration table transfers the electrical signal into vibrational signal (mechanical). The polysilicon resistor sandwiched in the cantilever receives the mechanical energy and converts it into an electrical signal. The signal domains were exchanged from the electrical to mechanical and to electrical finally. This procedure needs

a time delay. If the sweeping rate is too fast (or the sweeping time in the frequency region is too short), the system's time delay will affect the results.

The whole system's delay time was investigated. At the range of a sweeping frequency, the oscillation spectra were recorded at different sweeping rate. The ratio of the sweeping range to the sweeping time was defined as sweeping rate, which indicates how fast the frequency of the input signal changes. The linear sweeping manner, that is the frequency changes linearly with the time, was selected. The sweeping direction can be either forward, the frequency changes from low to high value, or reverse, the frequency changes from high to low. The data of the both sweeping directions were compared.

Figure 23 (a) and (b) show the spectra of forward and reverse sweeping at different sweeping rate, respectively. Based on these spectra, the measured resonant frequency and the amplitude of spectra are the function of the sweeping rate, which are shown in Figure 24 and Figure 25 respectively. We can notice that the measured resonant frequency will change if the sweeping rate is higher. It is shifted towards the sweeping direction, that is the measured resonant frequency increases as the sweeping rate of forward sweeping is increased, and it decreases while the sweeping rate of reverse sweeping is increased. But in the low sweeping rate range, the measured resonant frequency and amplitude of spectra are stable. In terms of these results, the measured quality factor of the resonant system is a function of the sweeping rate, which is illustrated in Figure 26. When the sweeping rate is increased, the measured Q factor decreases. This indicates that the system cannot follow the change in the frequency if the sweep rate is too fast. One other thing that can be noticed is that the measured Q factor in the case of the reverse sweeping is lower than that of the forward sweeping. This could be attributed to the moment of the cantilever. During reverse sweeping, the frequency is changing from high to low. At a higher frequency point, the moving parts have a higher energy. When the frequency is changed to a lower

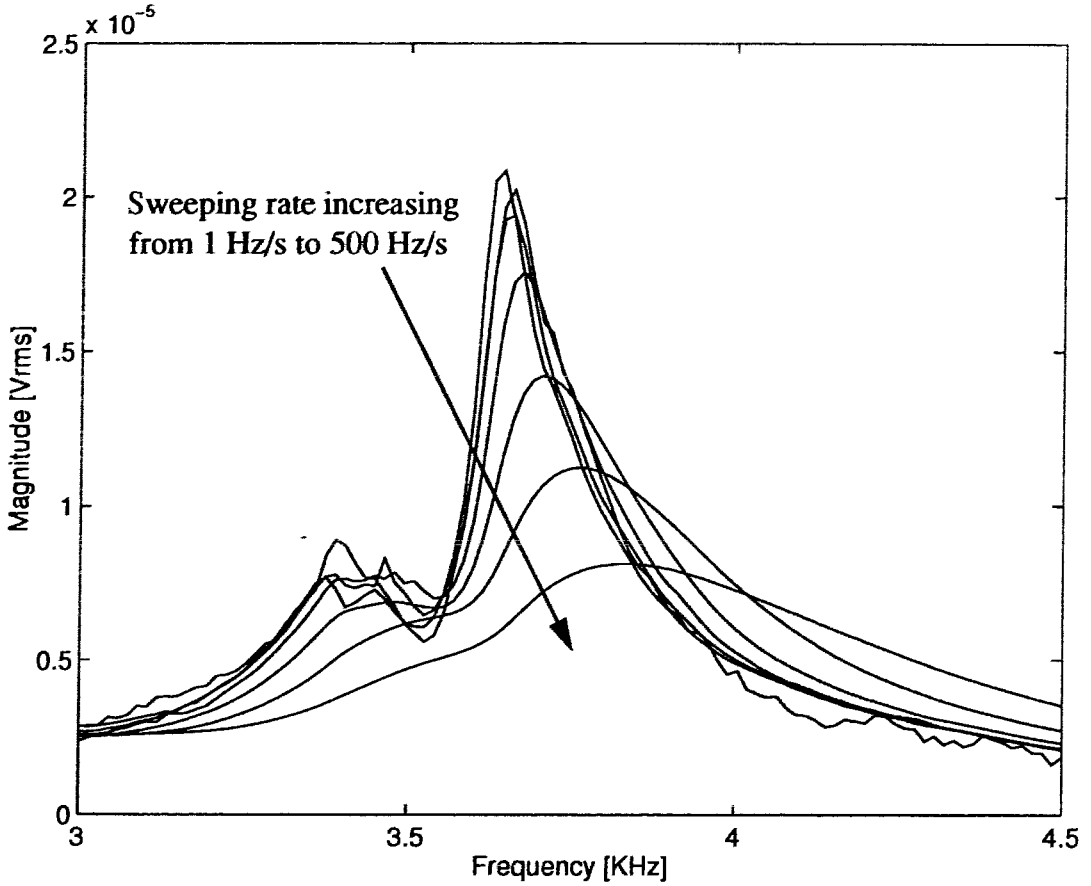

Figure 23(a): Spectra for forward sweeping at different sweeping rates

point, the energy of the moving parts is lost by damping and friction. But in the forward sweeping, the frequency is changing from low to high. The moving parts obtain their increasing energy from the electrical signal source. The losing energy of the moving parts in the case of the reverse sweeping is much slower than receiving the energy in the case of the forward sweeping. So, the moving parts have the different response time for forward

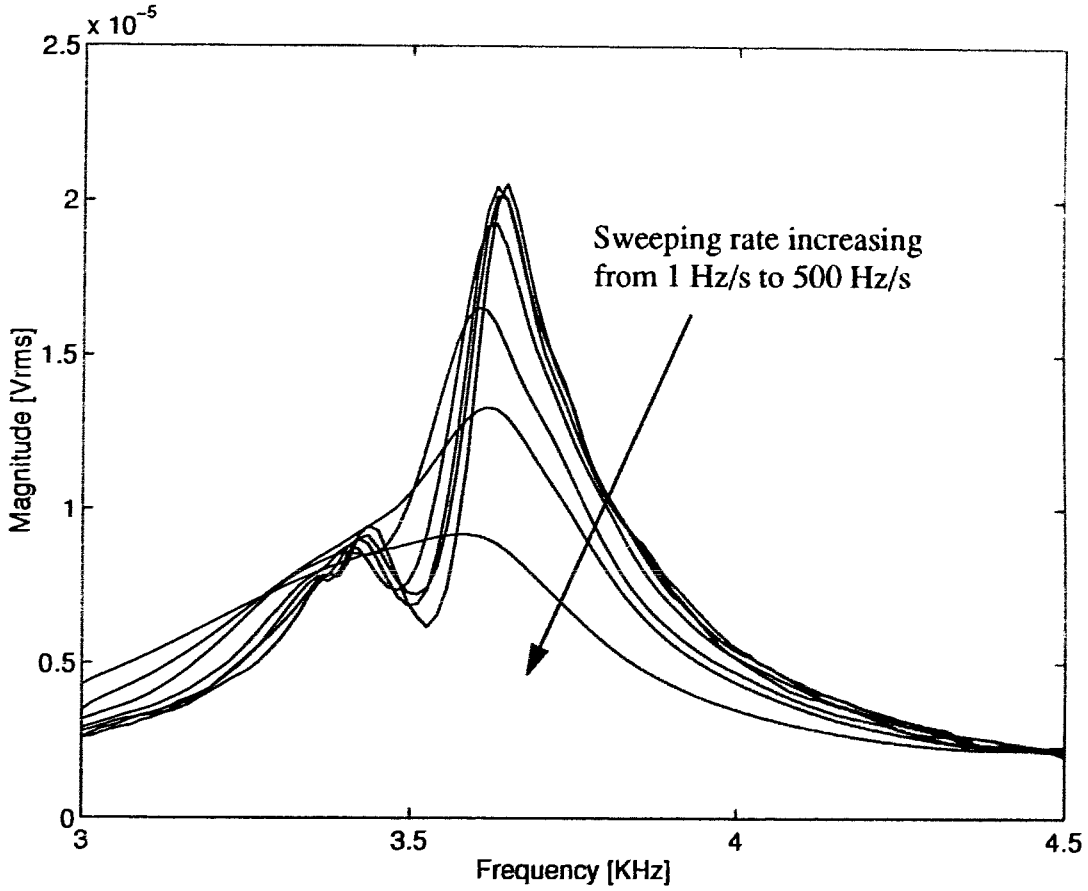

Figure 23 (b): Spectra for reverse sweeping at different sweeping rates

and reverse sweeping. The slower loss of energy in reverse sweeping makes the resonant curve wider, and so, the measured Q factor is lower than that in the forward sweeping.

In order to get accurate results, the forward sweeping should be selected. Further, lower sweeping rate is better, however, this will increase the testing time. 3 Hz/s is a very good

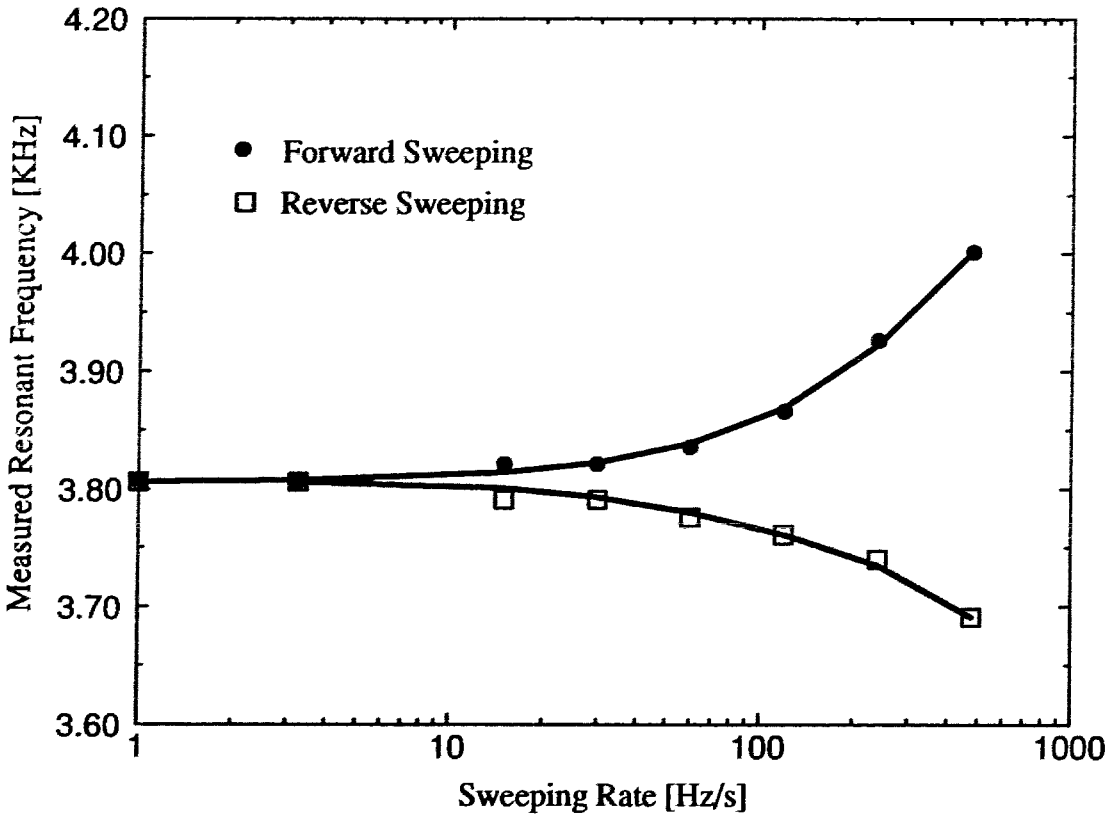

Figure 24: Measured resonant frequency vs. sweeping rate

sweeping rate for the measurement. Fixing the sweeping rate is important or else the shift in the resonant frequency will be introduced and this might contribute to error in measurement.

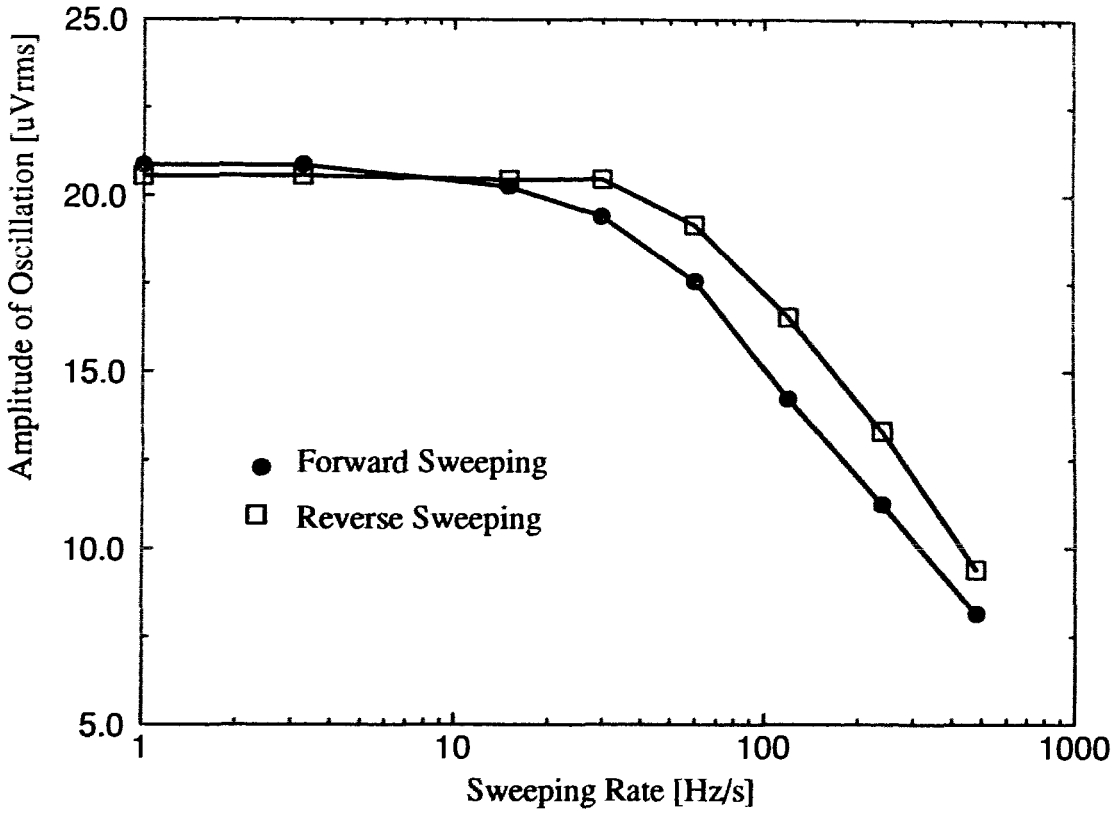

Figure 25: Amplitude of oscillation spectra vs. sweeping rate

6.1.3 Bias Voltage Effect

The electrical resistance of the polysilicon resistor sandwiched in the cantilever is changing while the cantilever is vibrating. One simple way to measure the resistance is to connect the four resistors in a bridge configuration. A bias voltage has to be applied to the bridge. One node in the bridge with a fixed potential is connected to a input of the differential amplifier and the other point (with changing potential when vibrating) is connected to the other input. As the cantilever is vibrating, the change in resistance will generate an

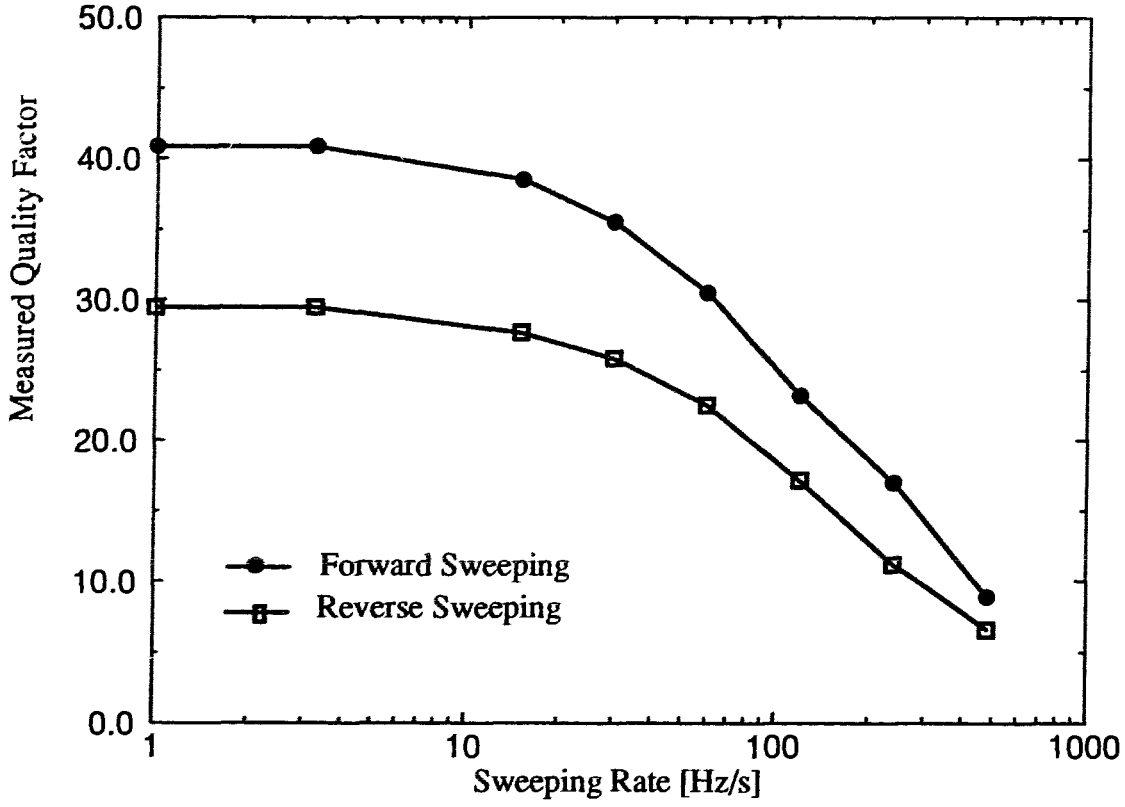

Figure 26: Measured quality factor as a function of sweeping rate

AC signal and it is amplified. So the bias voltage on the bridge will affect the AC signal, and therefore, it may affect the output.

Figure 27 (a) and (b) show the spectra at different bias. From the figures, we can notice that the bias voltage on the resistor bridge mainly affects the amplitude of the signal. The amplitude of the measured spectrum becomes lower as the bias voltage is decreased. This is due to the output of the bridge (AC signal) is directly proportional to the bias voltage on the bridge. It should be noted that the resonant frequency was not changed when the bias

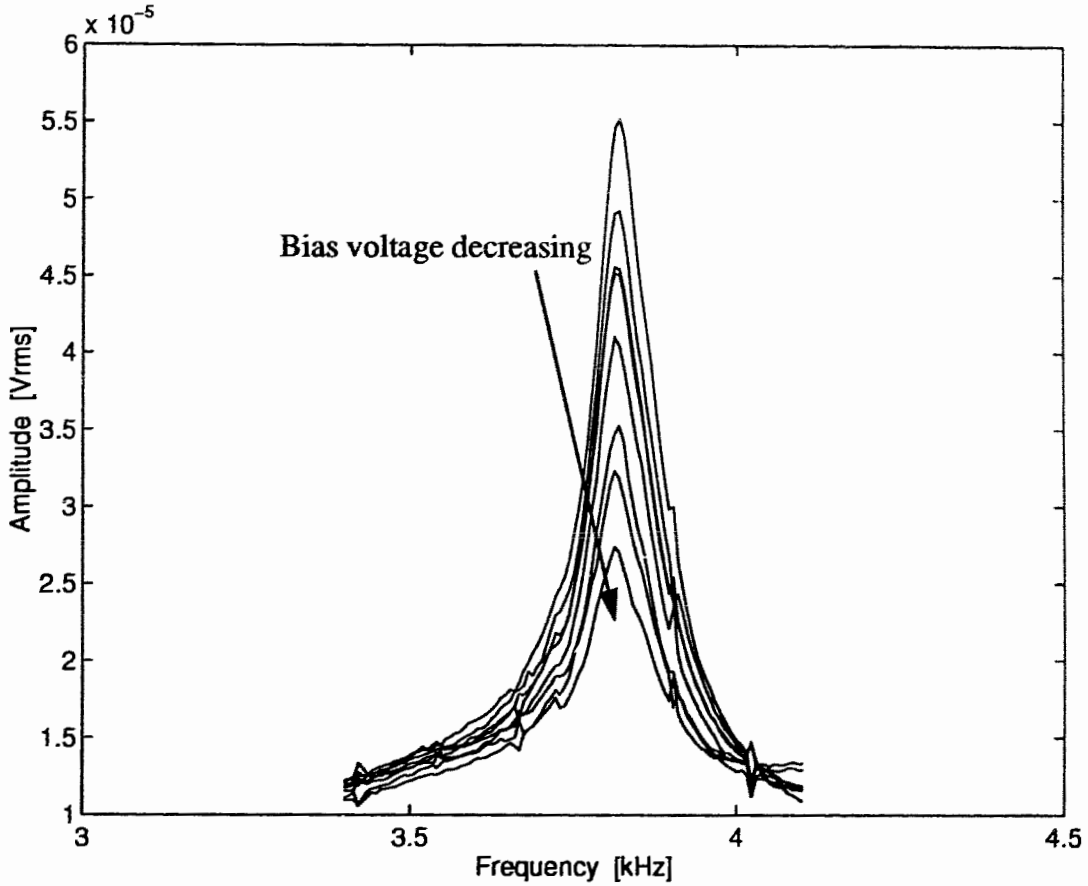

Figure 27 (a): Oscillation spectra at different bias voltages on resistor bridge

changed in the range from 0.4 V to 3 V.

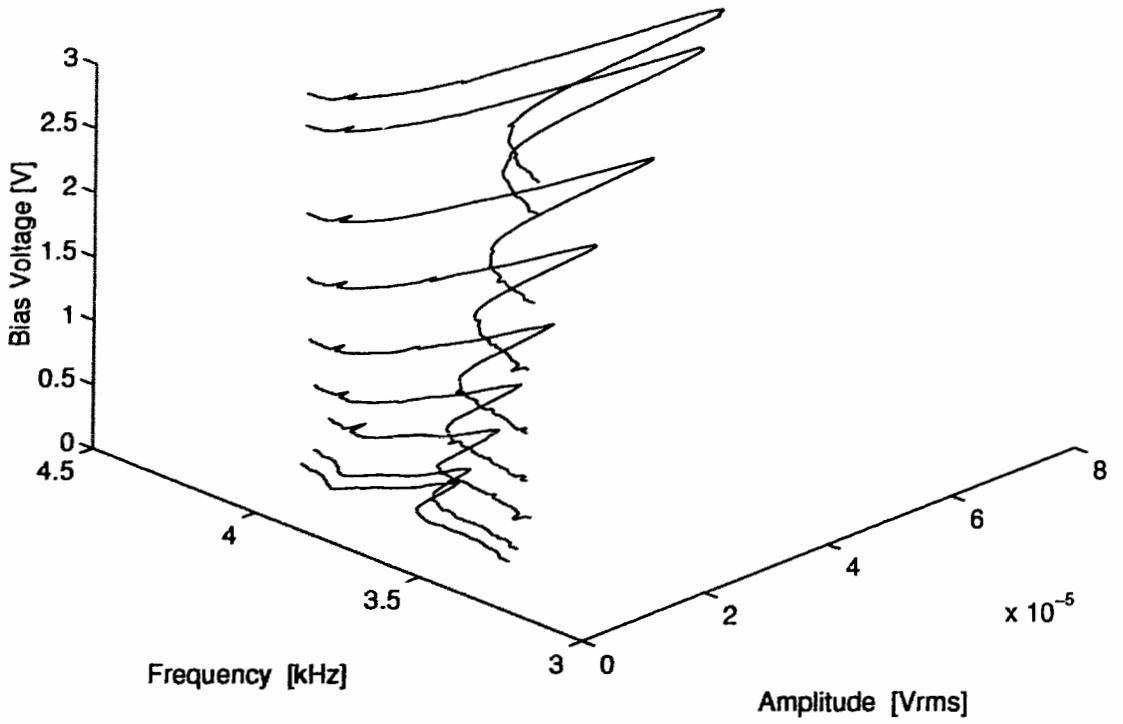

Figure 27 (b): A three axis plot of the spectra at different bias voltages

6.2 Calibration with Polystyrene Spheres

6.2.1 In Air Measurement

The mass sensing experiment in air was performed using polystyrene spheres. The resonant frequency of the unloaded cantilever was first tested. And then, spheres were placed on the pay-load platform of the cantilever with micromanipulator. The electrostatic force

was sufficient to secure the spheres to the platform, as shown in Figure 21. The resonant frequency of the cantilever loaded with the spheres was measured. The oscillation spectrum was shifted due to the loaded mass. Figure 28. shows the shift in the oscillation spec-

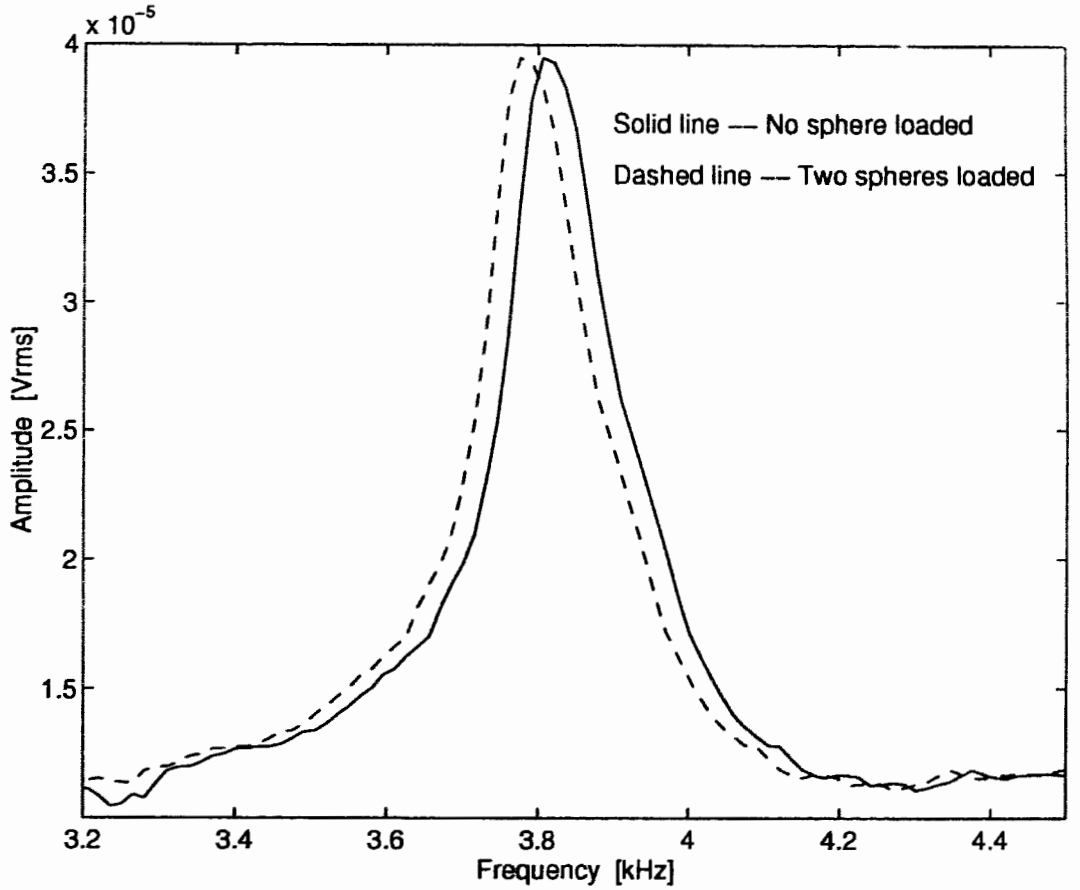

Figure 28: Shift in resonant frequency for 1.172 ng mass loading (in air)

trum after two polystyrene spheres were loaded. The in-air calibration results are listed in

Table 3. The results indicate a mass sensitivity of about 25 Hz/ng.

6.2.2 In Liquid Measurement

Mass sensing experiment in liquid medium was performed with polystyrene spheres in DI water. A liquid tank was constructed and a hole was drilled on one side of the tank. The hole was covered with a thin rubber membrane in order to insert the axis of the vibration table without producing any liquid leakage. The tank could hold 3 litres of DI water. If the water volume is too less, the ripples and waves formed on the surface will affect the movement of the cantilever structure. This appears as noise in the signal. The measurement should be performed in a still liquid with the device located more or less in the center of the tank.The cantilever structure electrically insulates the polysilicon resistor. However the bonding pads and external connection wires were covered by an epoxy to provide insulation.

The results from the experiments conducted in DI water are listed in Table 3. One sphere loading can lead a shift of 14 Hz in resonant frequency, which results in a sensitivity of 23 Hz/ng. It is slightly less than in air response. Figure 29 shows the shift in measured spectrum in DI water.

Table 3: Calibration Results with Polystyrene Spheres

	One Sphere	Two Spheres	Four Spheres
Resonant Frequency Shift in Air [Hz]	15	30	60
Resonant Frequency Shift in DI Water [Hz]	14	26	49

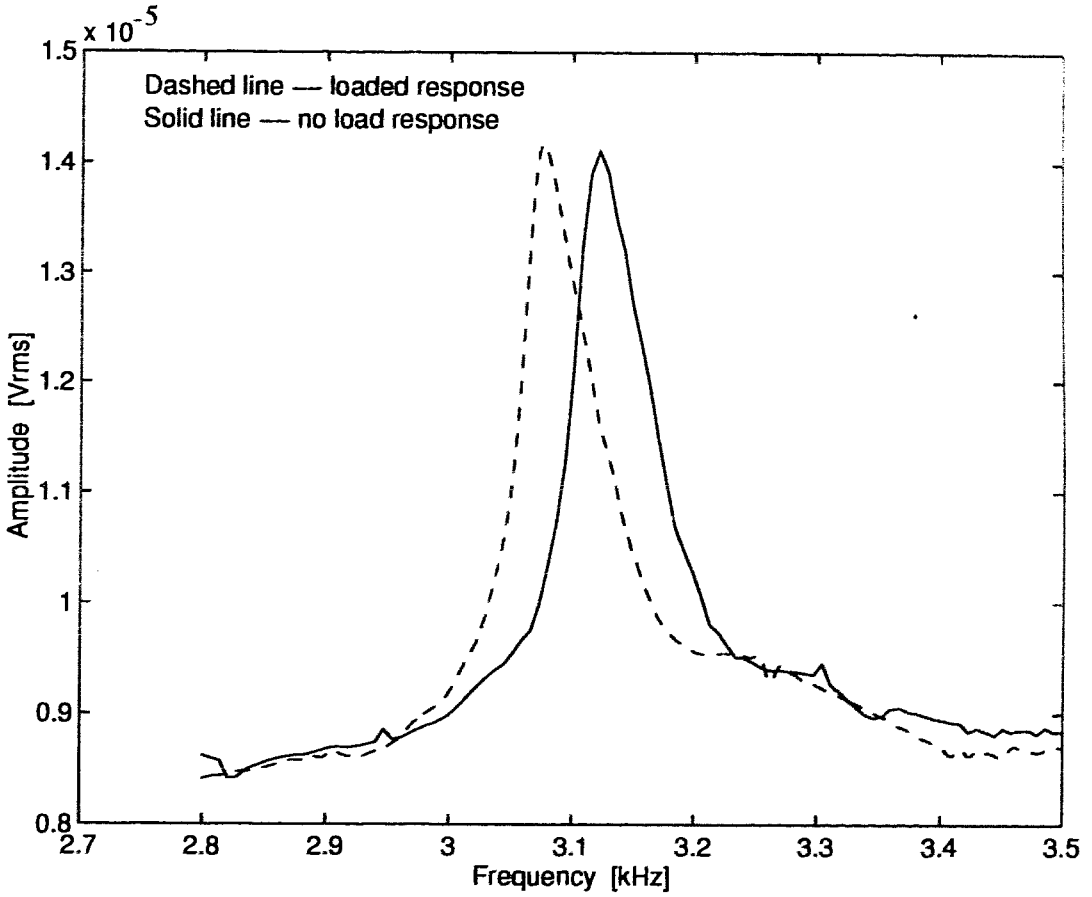

Figure 29: Shift in resonant frequency for 2.344 ng mass loading (in DI water)

The resonant frequency in air was different compared to the resonant frequency observed in DI water. The cantilever in air had a resonant frequency of 3.806 KHz, while the resonant frequency of 3.122 KHz was observed in DI water. This could be attributed to the increased damping experienced by the cantilever structure when oscillating in liquid medium.

Chapter 7

Application

The CMOS-compatible micromachined mass resonant sensor developed in this thesis work has potential applications.

7.1 Biomass measurement

The sub-nanogram mass sensor has application in measuring individual discrete masses of less than 10 microns in diameter. Since the piezoresistivity of polysilicon was used, the measurement set-up is simpler compared to the original technique of the mass sensor. The reading resolution can be increased with a good lock-in amplifier. A resolution of 0.1 ng can be readily achieved.

At present, the study of single biological cells is a promising application for such small discrete sensors. Microbiologists and biomedical engineers are interested in how cells live and grow under various conditions. Studies of cell growth and division and the reaction of cells to toxic substances are a couple of examples among many possible applications. Currently the cell mass is determined using bulk measurement of dehydrated cells [18]. This technique is destructive test which is statistical in nature. Another approach proposed by Kilburn et al. [19] suggested the use of acoustic resonance densitometry to measure the total mass of cell cultures with in excess of 10^6 cells per ml. The discrete mass sensor will have advantages over both of the above methods as it will monitor the mass of a single cell non-destructively.

Cell studies are largely performed in a liquid culture, thus most applications will require in fluid measurement. The device reported here can work in fluids and this makes it possible to monitor the growth of cells in culture fluids. The cantilever sandwiched in with a polysilicon resistor and the on-chip electronic circuit may form a smart sensor which can monitor the growth of the biocells in real time.

7.2 Physical Sensor

The resonant frequency of a solid body is related to the damping in addition to the structural parameters. If the device is working in different medium, the resonant frequency will be shifted. Pressure/vacuum sensors and liquid density sensors are other applications where the subnanogram measurement system can be utilized. For this application, the cantilever structure should have an increasing drag so that the sensitivity can be higher. This can be achieved by increasing the size of the payload platform.

7.3 Chemical Sensor

As a resonant sensor, the device can be a chemical sensor if a special material is coated on the surface of the cantilever. For instance, a polymer, which can absorb humidity, is coated on the surface to absorb humidity, thus the resonant frequency will change due to ambient humidity level. Since the cantilever structure is very flexible and CMOS polysilicon gate has good piezoresistance, very sensitive and smart sensors can be implemented.

Chapter 8

Conclusion

An application of CMOS-compatible micromachining for potential biological and chemical applications has been demonstrated in this thesis. The micromachined silicon dioxide cantilever sandwiching a polysilicon resistor was employed as a resonant sensor to measure the mass of discrete objects. The mass measurement of discrete objects of diameter 10 μm and mass of less than 1 ng shows the principle of subnanogram discrete mass sensing. The measurement of such minute discrete objects opens many possible applications in biotechnology. The technique developed in this thesis work offers the possibility of monitoring mass fluctuations of individual living cells in the culture fluid and it would be a valuable tool to bioengineers studying cell growth under various conditions.

The piezoresistance of polysilicon gate material in commercial CMOS technology was investigated. The results show the polysilicon gate material in CMOS process has a good piezoresistance characteristics. The gauge factor of 25 (MITEL1.5 CMOS) and 24 (NT CMOS3) can be obtained. Using the piezoresistance of the polysilicon, the resonant frequency of the cantilever sandwiched in with a polysilicon resistor can be easily tested. Further, the device can be operated inside a liquid medium.

The measurement set-up for testing the resonant frequency of the cantilever was configured using a miniature vibration table to excite the cantilever to oscillate. Electrical signal output from the resistor bridge was detected with SR850 Lock-in Amplifier, which can display and record the data and the resonant frequency can be determined accurately.

The cantilever fabricated using CMOS-compatible micromachining technique resonated

at 3.806 KHz in the fundamental mode. A Q factor of 41 in air and 22 in DI water was obtained. The sweeping rate of the driving signal has an effect on the measured resonant frequency and amplitude of the spectrum. Increasing the sweeping rate will result in decreasing the Q factor. For accurate measurement, the sweeping rate should keep at low rate.

Polystyrene spheres were loaded individually onto the tip of the cantilever and the resonant amplitude versus frequency characteristic was obtained both with and without a load and both in air and in DI water. An experimental mass sensitivity of 25 Hz/ng in air and 23 Hz/ng in DI water were observed.

The new resonant structure presented in this work has proven that there are two main advantages in this device. One is that the device can work in liquids. That makes it possible for bioengineers to monitoring the growth of cells in a culture fluid. The second is that the sensor part can be easily combined with CMOS signal processing circuits to fabricate smart sensors.

Appendix A:

ANSYS Simulation

ANSYS5.0 is a finite element analysis software package, a general mathematical method of modelling physical problems with complicated domains and boundary conditions. It includes Static Analysis, Modal Analysis, Harmonic Analysis, Thermal Analysis and so on. The stress distribution induced by a force, a pressure or a displacement is predicted with the Static Analysis. Modal Analysis shows the resonant frequencies and mode shapes of the resonant microstructure. The amplitude versus frequency response characteristics was found using the Reduced Harmonic Analysis.

The analysis procedure in ANSYS is divided into three sections. The first section is pre-processing in which the complete model of the structure is defined. This definition includes material properties, model geometry, and division into elements and nodes (mesh). The second section, solution, constructs the matrix equation from the model and solves it for the nodal values. In this section, the analysis type and analysis options are defined and the boundary conditions are set up. But in ANSYS version 4.4A, the definition of analysis type and options and set-up of the boundary conditions are proceeded in section of preprocessing. The solution requires very little operator input. Post processing is the final section, in which the raw solution data are used to generate graphs and contour images in order to make the results more meaningful. The analysis flow diagram is shown in Figure A.1.

In the thesis work, ANSYS 5.0 was used to simulate the stress distribution, resonant frequency of the cantilever and the shift in resonant frequency with loaded discrete masses. Section A.1 explains the procedure for getting the stress distribution according to the displacement of the cantilever tip. Section A.2 and A.3 show the procedure used in modelling

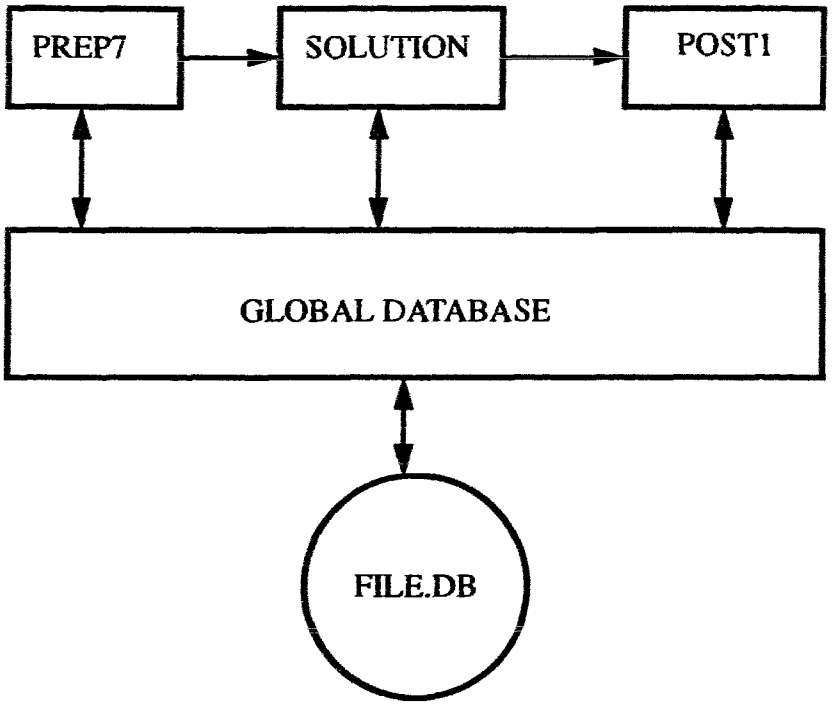

Figure A.1: ANSYS analysis flow-chart

the resonant frequency, oscillation spectrum and resonant frequency shift. The detailed listings of all input and output are provided in Section A.4.

A.1 Stress Analysis

The stress analysis is performed using Linear Static Analysis, which is the default. We do not need to enter analysis type or options in this simulation. The detailed listing of all input and output for the stress analysis is put in section A.4.1. To entering the ANSYS program, the command "ansys.e" is executed. When the program tells you "begin". you may

type in "/show,x11" followed by "/menu, on" command. At this moment, ANSYS window system should be shown on the screen. The menu on the screen can be selected with mouse and on-line help is available. For the cantilever structure, the element type of "et 45", a three dimensional brick structural with 8 nodes at the corners was selected. The "mp" command was used to define the material properties of Young's modulus and density for silicon dioxide and polysilicon. For simplicity, the basis units of grams and centimeters were used. A three dimensional solid model of the cantilever was defined graphically. As shown in Figure A.2 the solid model consists of 81 volumes, each volumes

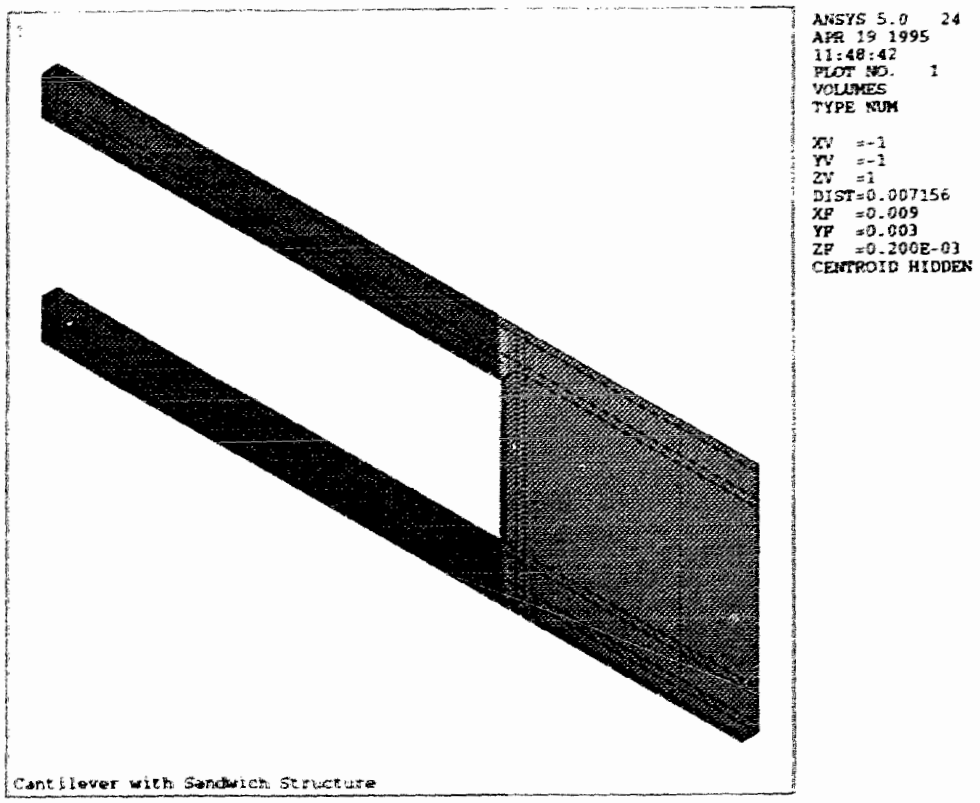

Figure A.2: Solid model of the cantilever for ANSYS simulation

defined by 8 key points. Between two key points, a line is defined.

The elements are defined by segmenting each line manually using the line division command ("ldvs"). The lines are segmented into 10 μm sections if the length of lines is greater than 10 μm. If its length is shorter than 10 μm, it is divided into two segments. Elements and nodes are generated over the solid model using the volume mesh command "vmesh" on each volume. Before mesh, the material reference number should be designated to the volume with the "mat" command, or it will default to number 1 material. Figure A.3 and

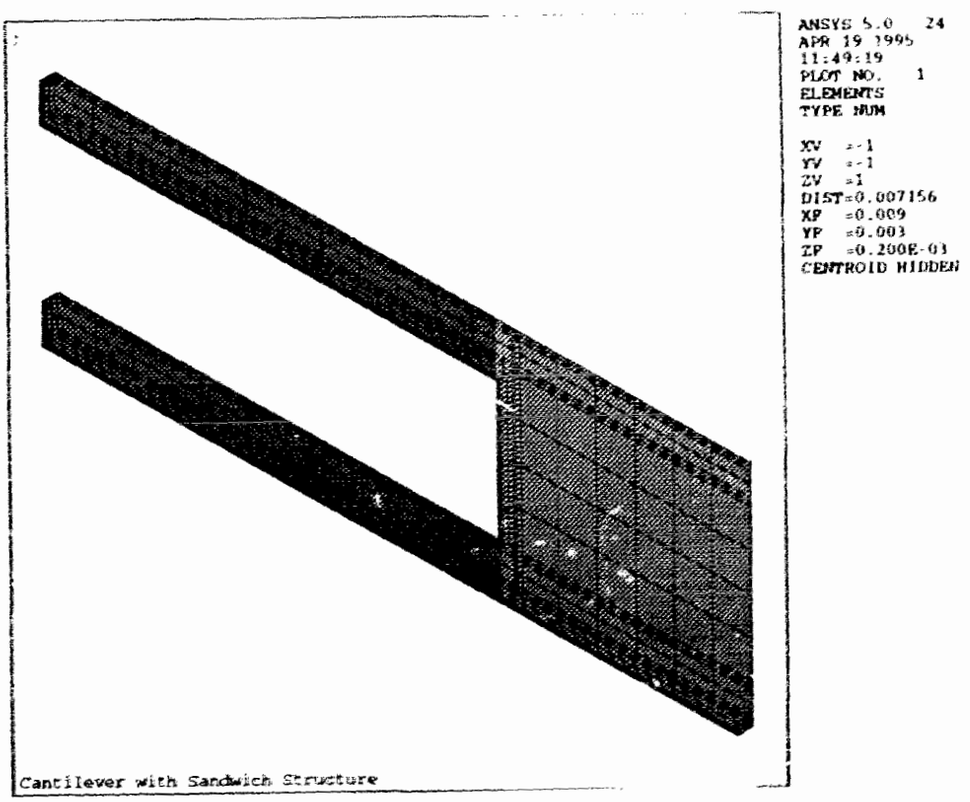

Figure A.3: Element model in ANSYS

Figure A.4 show the generated elements and nodes, respectively.

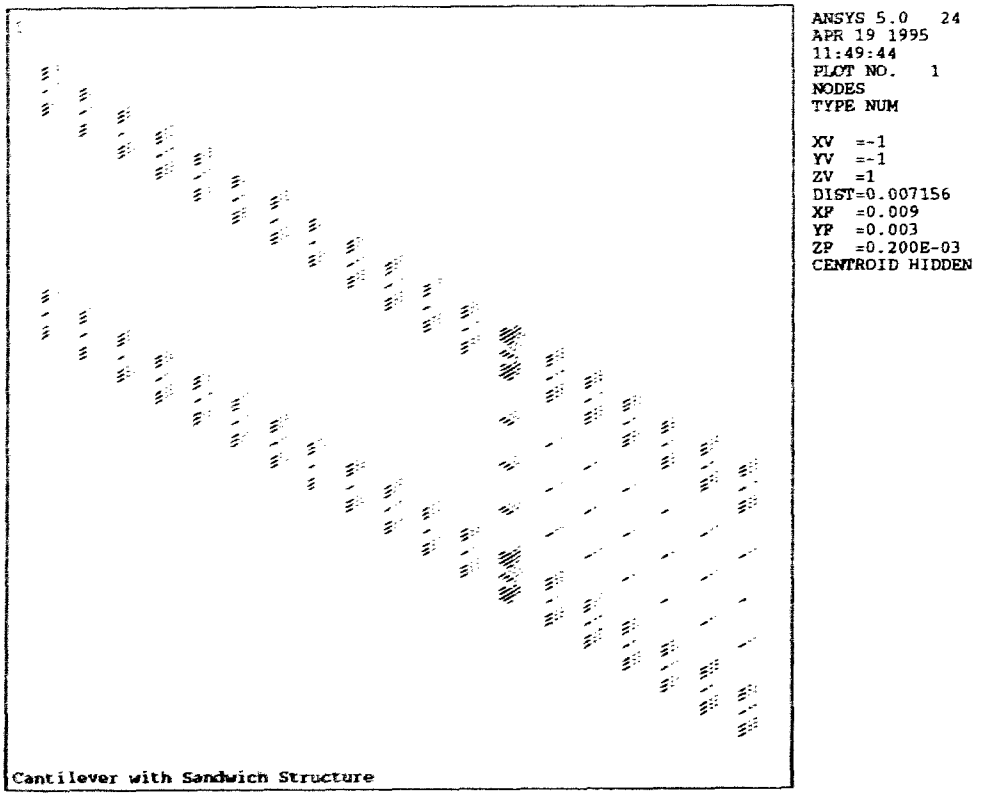

Figure A.4: FEA nodes

The boundary condition is to clamp the base of the cantilever beams in three translational dimensions and three rotational dimensions. Two forces are to act on the tip corners of payload platform of the cantilever in order to make the cantilever deformed. By adjusting the forces, a certain amount of displacement, equal to the amount of the testing point, can be achieved.

In postprocessing, a path can be defined using "lpath" command. Along this path, a displacement distribution or a stress distribution can be calculated with the command "pdef",

and can be plotted using "plpath" command. Figure A.5 and Figure A.6 give the exam-

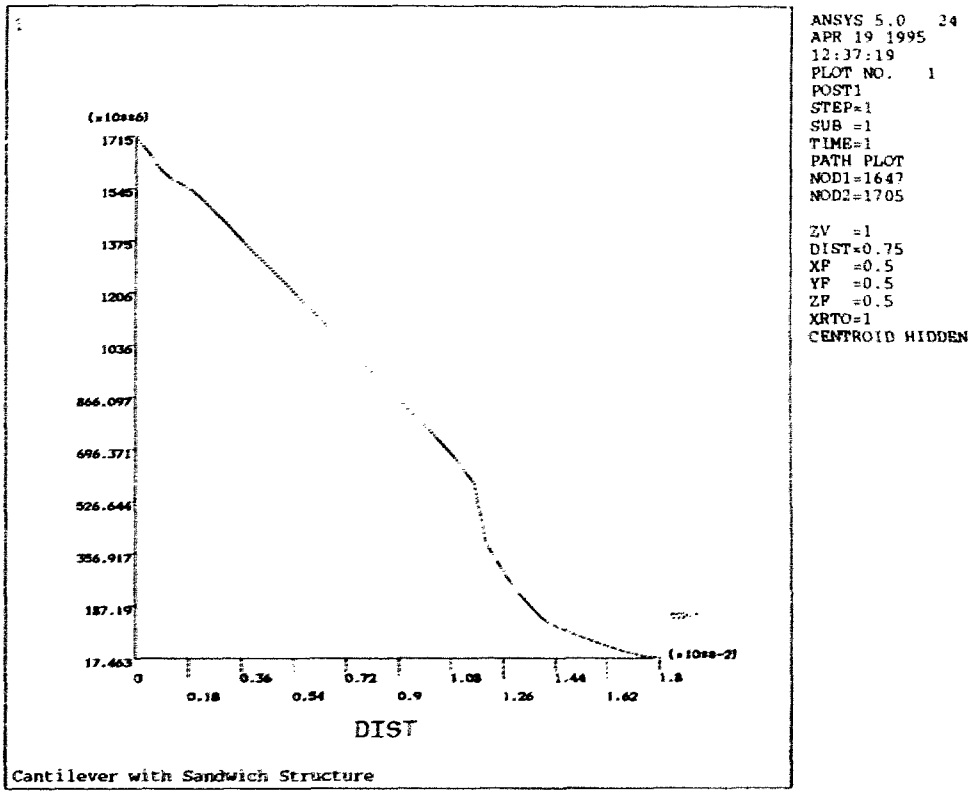

Figure A.5: Stress distribution along the top surface of cantilever

ples of "plpath", which are the stress distribution along the cantilever beam on the top surface and the bottom surface of the beam, respectively. Figure A.7 shows the displacement of the cantilever and Figure A.8 presents the stress distribution along the path vertical to the beam at the base. It illustrates that the stress changes from negative value (compressive) at the bottom part to positive (tensile) at the top part when the cantilever bends down.

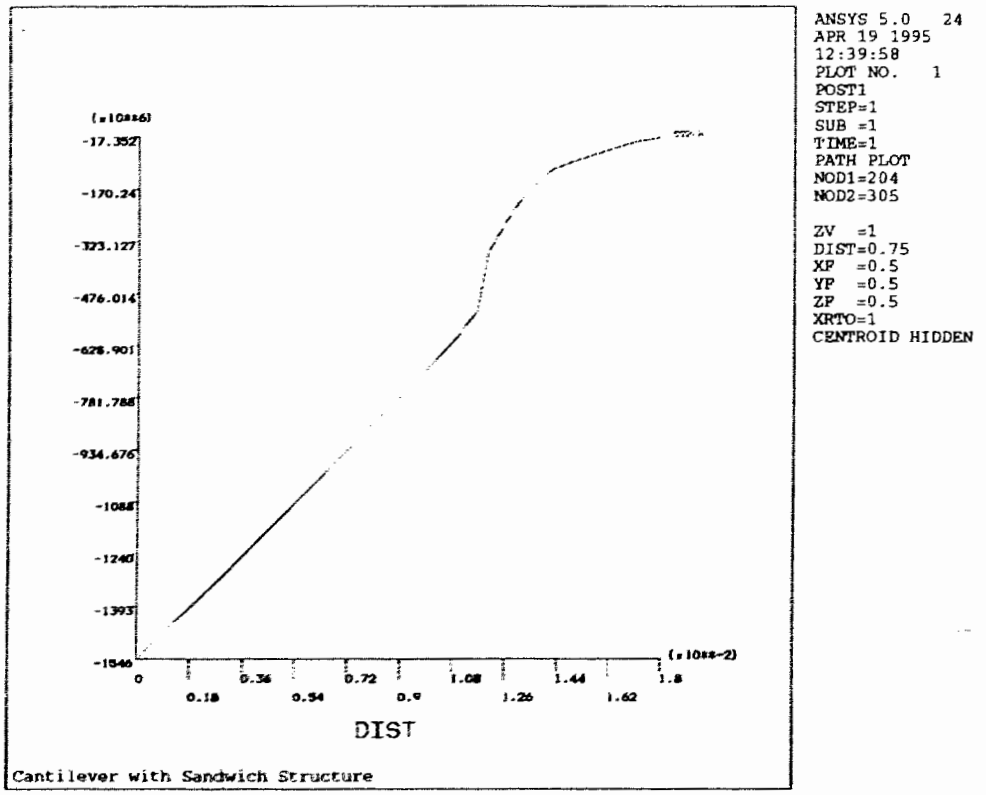

Figure A.6: Stress distribution along the bottom of cantilever

A.2 Modal Analysis

The resonant frequencies and the mode shapes of a solid model can be achieved with Model Analysis. In the modal analysis, the generation of the solid model of the cantilever is as same as in the static analysis. It is convenient to copy the solid model of the cantilever from the static analysis.

The input list of the modal analysis is provided in A.4.2. Mass loading can be modeled using the point mass element (mass21) located at the middle of the tip of the cantilever. This mass element is put on one shared node with the cantilever structure by "e" com-

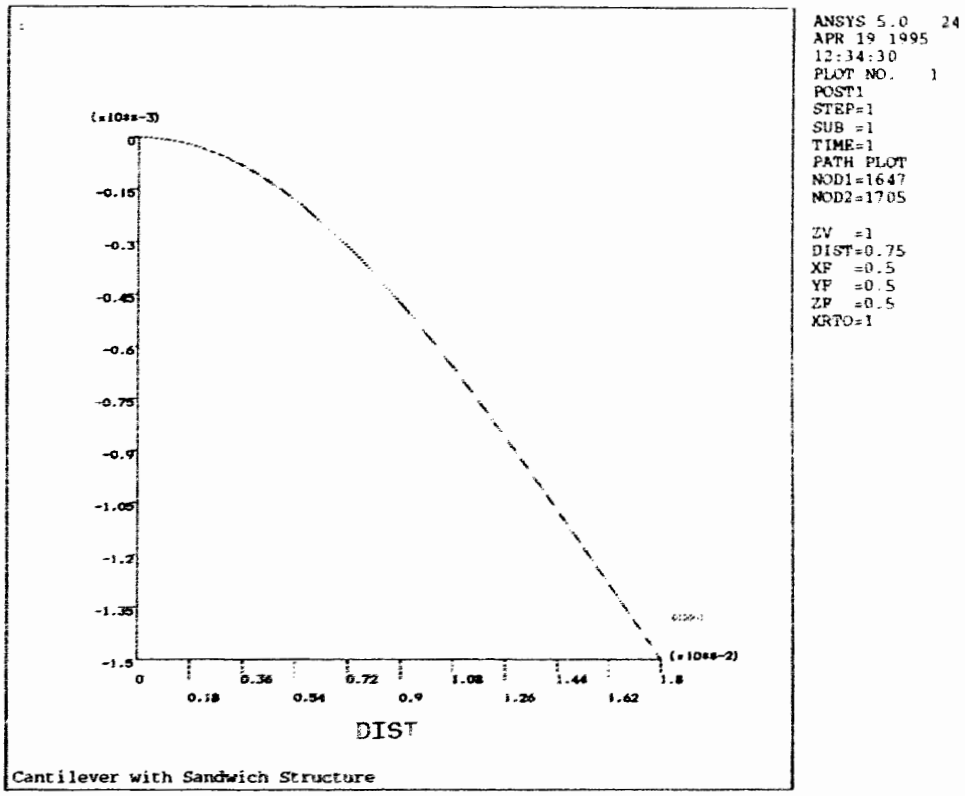

Figure A.7: Displacement of the cantilever beam

mand. Thus the point mass will affect the solution of the model. The value of the point mass may be defined by the real constant command "r".

The only boundary condition applied to this model is to clamp the base of the cantilever in all dimensions. This simulates the clamping base of the cantilever due to its rigid connection to the substrate. This boundary condition is applied by constraining the all degrees of the freedoms at the base nodes with "D" command. The analysis type is defined with the Panel or command "ANTYPE, MODAL".

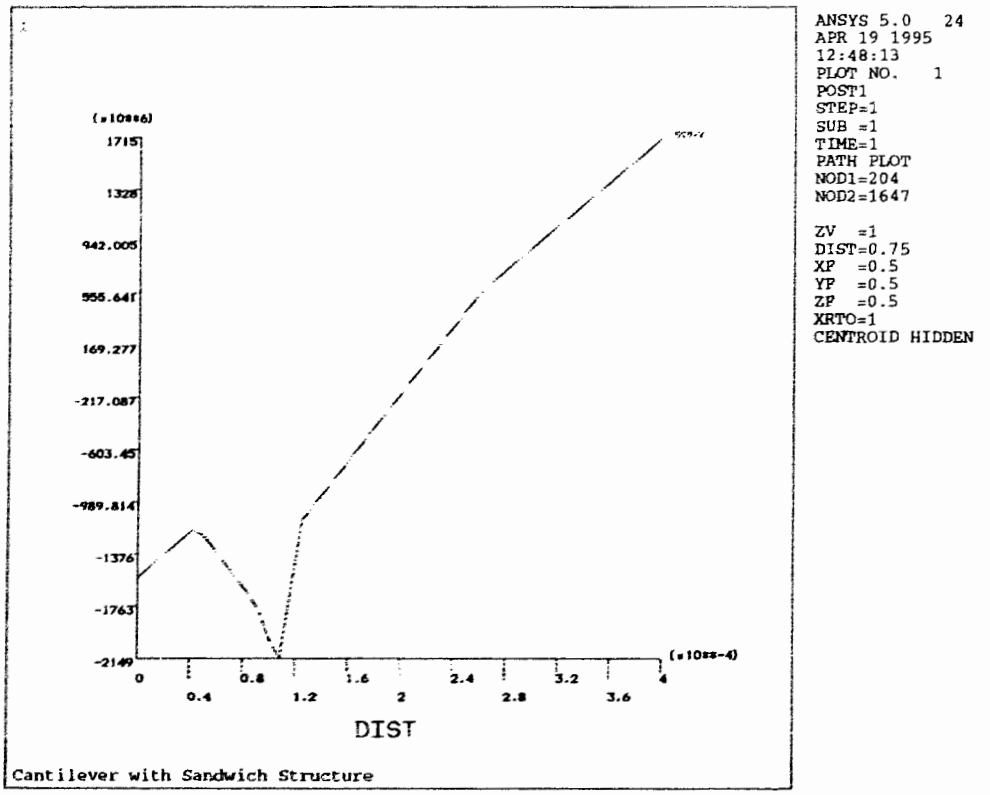

Figure A.8: Stress distribution along the direction from bottom to top at the base of the cantilever

For determination of resonant frequencies and mode shapes, master degree of freedom (master DOF). A master degree of freedom is an individual degree of freedom on a node which is considered more important. These master DOF's are monitored by ANSYS. Improper selection (too few or bad distribution on the structure) of master DOF's could result in missed resonances. But if too many master DOF's, the time for solution could be too long and the file of the result data could be so big that it could cause the computer stop running. In this simulation, 37 master DOF's were selected and they were uniformly located along the two beams and on the payload platform.

The solution was postprocessed using the module "/post1". The first resonant frequency data is loaded with "set,1,1" command. The plot of the fundamental mode shape shown in Figure A.9 is generated using the command "pldisp,2". The torsional resonant mode data

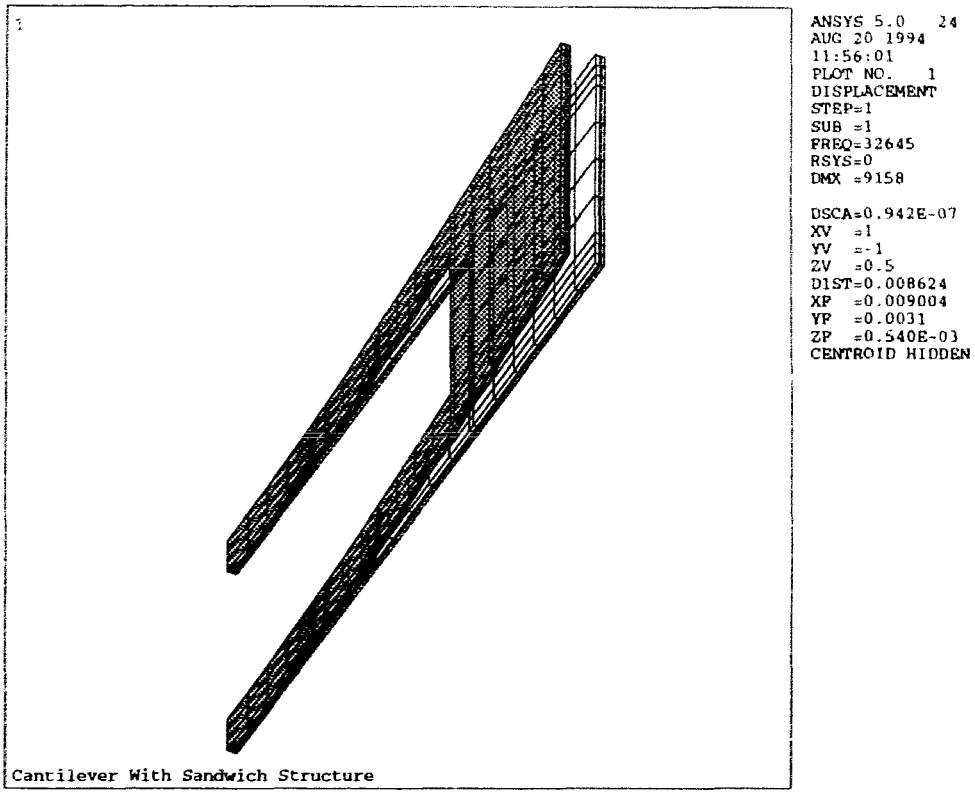

Figure A.9: Fundamental mode shape

can be loaded with "set,1,2" and the first harmonic mode shape can be obtained with "set,1,3". Figure A.10 and Figure A.11 present these two mode shapes respectively.

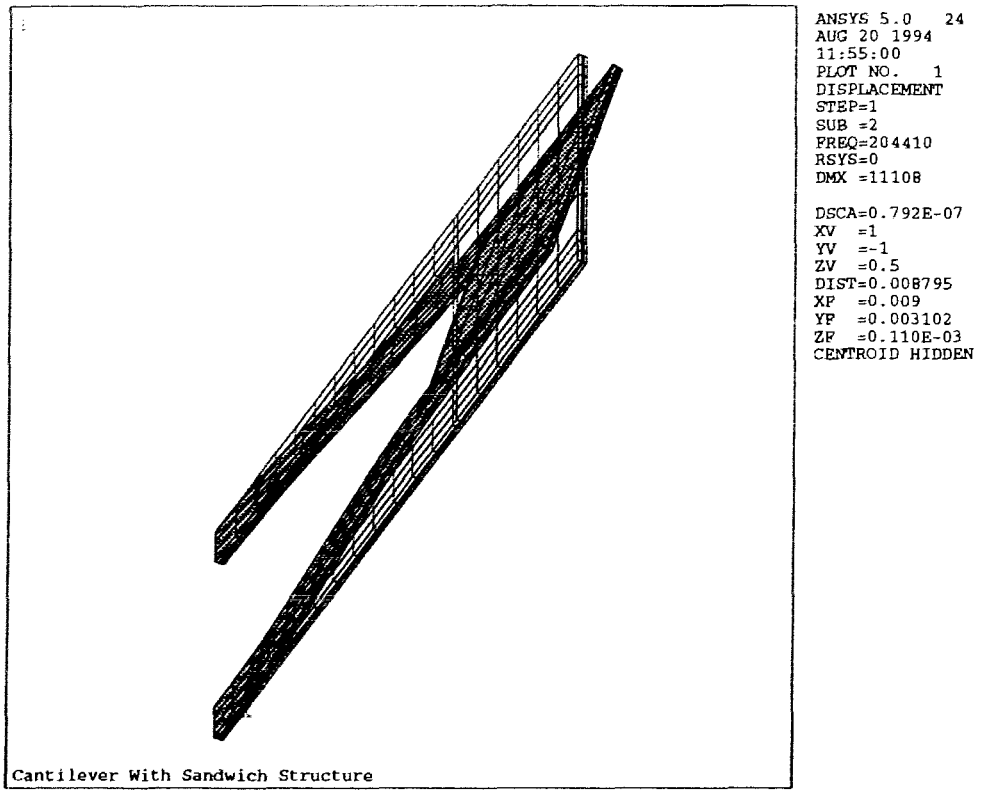

Figure A.10: Torsional vibration mode shape

A.3 Reduced Harmonic Analysis

The input listing for the reduced dynamic analysis is provided in section A.4.3. With this analysis, defined with the command "ANTYPE,HARM", the resonant spectrum of a point on the structure can be modelled. This analysis uses the same finite model formulated for the modal analysis and has to be based on the results of the modal analysis.

The displacement of the cantilever tip over a range of frequency from 3500 Hz to 5500 Hz was desired. The range of frequency was defined with "HARFRQ" command. In order to

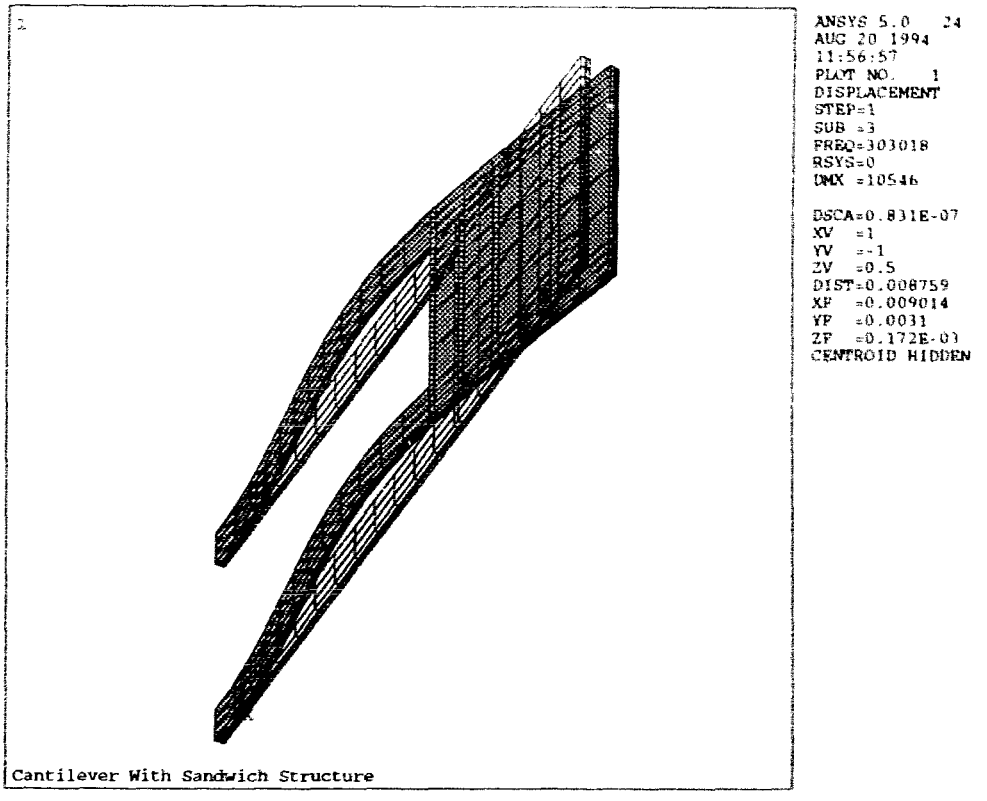

Figure A.11: First harmonic mode shape

obtain the mass shifted and unshifted resonant curve on the same graph, a copy of the modeled cantilever with a mass load was made beside the original cantilever. Both cantilevers were given two forces acting on the tip corner nodes to excite the cantilevers to vibrate at the given frequency.

The post processor "/post26" was used to view the graph of the displacement versus frequency for a node on the tip of both cantilevers. The result data file was loaded with the command "file,,rfrq" and the specific node was defined using "NSOL" command. The graph was drew with "PLVAR", and it is shown in Figure A.12.

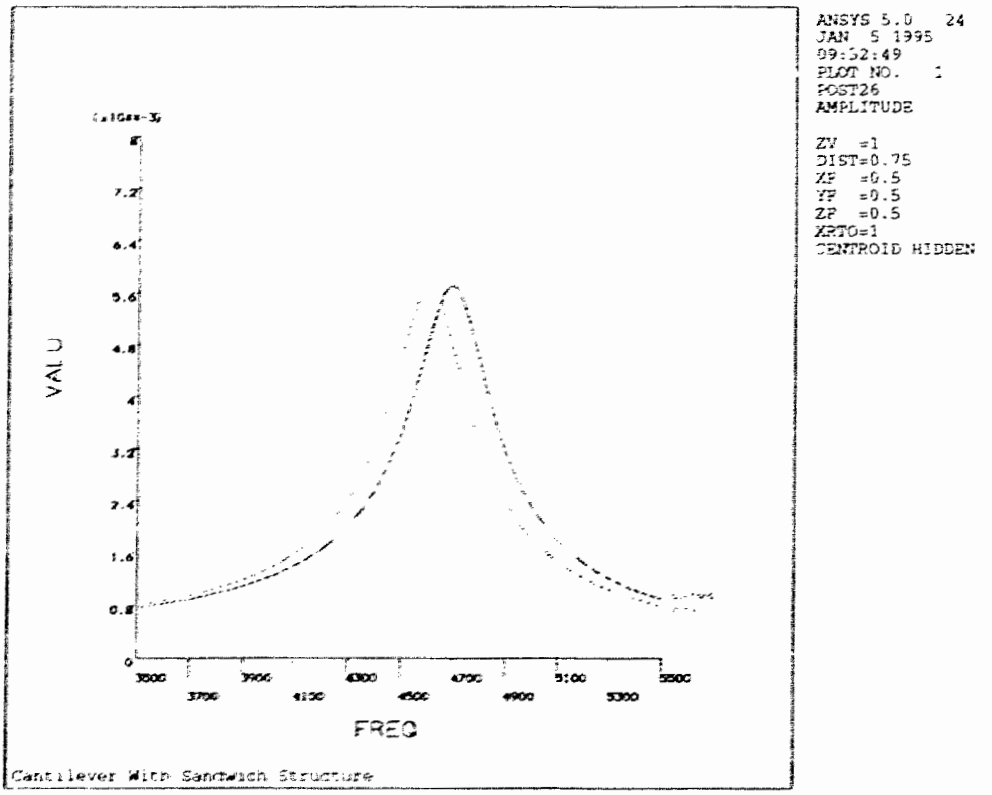

Figure A.12: Shift in resonance due to mass loading

A.4 Input Listing for ANSYS Simulation

A.4.1 Input Listing for Static Analysis

********** ANSYS INPUT LISTING (file.log) **********

```
/COM,ANSYS REVISION 5.0 24 16:18:25 04/13/1995
/show,x11
!/menu,on
/PREP7
/TITLE,Cantilever with Sandwich Structure

/COM, INPUT MATERIAL DATA AND ELEMENT TYPE DEFINITION
MP,EX,1,5.7e11
MP,DENS,1,2.2
MP,DENS,2,2.3
MP,EX,2,1.9e12
```

```
ET,1,solid45

/COM, GENERATE SOLID MODEL
k,1
k,2,1.18e-2
k,3,1.2e-2
k,4,1.6e-2
k,5,1.8e-2
kplot
kgen,2,1,5,1,0,2.0e-4,0
kgen,2,1,10,1,0,8.0e-4,0
kgen,2,1,20,1,0,5.0e-3,0
kgen,2,1,40,1,0,0,0.9e-4
kgen,2,1,40,1,0,0,1.25e-4
kgen,2,1,40,1,0,0,4.0e-4
v,1,2,7,6,41,42,47,46
v,2,3,8,7,42,43,48,47
v,3,4,9,8,43,44,49,48
v,4,5,10,9,44,45,50,49
v,6,7,12,11,46,47,52,51
v,7,8,13,12,47,48,53,52
v,8,9,14,13,48,49,54,53
v,9,10,15,14,49,50,55,54
v,11,12,17,16,51,52,57,56
v,12,13,18,17,52,53,58,57
v,13,14,19,18,53,54,59,58
v,14,15,20,19,54,55,60,59
v,17,18,23,22,57,58,63,62
v,18,19,24,23,58,59,64,63
v,19,20,25,24,59,60,65,64
v,21,22,27,26,61,62,67,66
v,22,23,28,27,62,63,68,67
v,23,24,29,28,63,64,69,68
v,24,25,30,29,64,65,70,69
v,26,27,32,31,66,67,72,71
v,27,28,33,32,67,68,73,72
v,28,29,34,33,68,69,74,73
v,29,30,35,34,69,70,75,74
v,31,32,37,36,71,72,77,76
v,32,33,38,37,72,73,78,77
v,33,34,39,38,73,74,79,78
v,34,35,40,39,74,75,80,79
v,41,42,47,46,81,82,87,86
/view,1,1,1,-1
vplot
```

```
/view,1,1,1,1
vplot
vplot,28
v,42,43,48,47,82,83,88,87
v,43,44,49,48,83,84,89,88
v,44,45,50,49,84,85,90,89
v,46,47,52,51,86,87,92,91
v,47,48,53,52,87,88,93,92
v,48,49,54,53,88,89,94,93
v,49,50,55,54,89,90,95,94
v,51,52,57,56,91,92,97,96
vlist
v,52,53,58,57,92,93,98,97
v,53,54,59,58,93,94,99,98
v,54,55,60,59,94,95,100,99
v,57,58,63,62,97,98,103,102
v,58,59,64,63,98,99,104,103
v,59,60,65,64,99,100,105,104
v,61,62,67,66,101,102,107,106
v,62,63,68,67,102,103,108,107
v,63,64,69,68,103,104,109,108
v,64,65,70,69,104,105,110,109
v,66,67,72,71,106,107,112,111
v,67,68,73,72,107,108,113,112
v,68,69,74,73,108,109,114,113
v,69,70,75,74,109,110,115,114
v,71,72,77,76,111,112,117,116
v,72,73,78,77,112,113,118,117
v,73,74,79,78,113,114,119,118
v,74,75,80,79,114,115,120,119
v,81,82,87,86,121,122,127,126
vplot,55
v,82,83,88,87,122,123,128,127
v,83,84,89,88,123,124,129,128
v,84,85,90,89,124,125,130,129
v,86,87,92,91,126,127,132,131
v,87,88,93,92,127,128,133,132
v,88,89,94,93,128,129,134,133
v,89,90,95,94,129,130,135,134
v,91,92,97,96,131,132,137,136
v,92,93,98,97,132,133,138,137
v,93,94,99,98,133,134,139,138
v,94,95,100,99,134,135,140,139
v,97,98,103,102,137,138,143,142
v,98,99,104,103,138,139,144,143
```

```
v,99,100,105,104,139,140,145,144
v,101,102,107,106,141,142,147,146
v,102,103,108,107,142,143,148,147
v,103,104,109,108,143,144,149,148
v,104,105,110,109,144,145,150,149
v,106,107,112,111,146,147,152,151
v,107,108,113,112,147,148,153,152
v,108,109,114,113,148,149,154,153
v,109,110,115,114,149,150,155,154
v,111,112,117,116,151,152,157,156
v,112,113,118,117,152,153,158,157
v,113,114,119,118,153,154,159,158
v,114,115,120,119,154,155,160,159
vplot
save

/COM, MESH VOLUMES
LESIZE,ALL,1.0e-3
llist
LESIZE,ALL,,,2,,2
llist
MAT,1
VMESH,1,31
VMESH,35,37
VMESH,39,40
VMESH,42,44
VMESH,46
VMESH,50,81
MAT,2
VMESH,32,34
MAT,2
VMESH,38
MAT,2
VMESH,41
MAT,2
VMESH,45
MAT,2
VMESH,47,49
nplot
eplot
vplot
save

/COM, GENERATE PRINT FILES
/show,v-p
```

```
vplot
/show,unused
/show,x11
eplot
/show,e-p
eplot
/show,unused
/show,x11
nplot
/show,n-p
nplot
/show,unused
/show,x11

/COM, SOLUTION
/SOLU

/COM, DEFINE THE BOUNDARY CONDITIONS
NSEL,S,LOC,X,-.1e-4,.1e-4
nplot
D,ALL,ALL,0.0
nsel,all
nplot
save
NSEL,S,LOC,X,1.79e-2,1.81e-2
nplot
nlist
D,ALL,UZ,-1.5e-3
nsel,all
nplot
SOLVE
FINISH

/COM, POSTPROCESS
/POST1
set,1
pldisp
pldisp,1
/show,disp-15
pldisp,2
/show,unused
/show,x11
lpath,1647,1705
pdef,disp-l,u,z
plpath,disp-l
```

```
/view
plpath,disp-l
/show,disp-l
plpath,disp-l
/show,unused
/show,x11
pdef,str-t,s,x
plpath,stre-t
plpath,str-t
/show,str-t
plpath,str-t
/show,unused
/show,x11
lpath,204,305
pdef,str-b,s,x
plpath,str-b
/show,str-b
plpath,str-b
/show,unused
/show,x11
lpath,244,310
pdef,str-p,s,x
plpath,str-p
/show,str-p
plpath,str-p
/show,unused
/show,x11
lpath,204,1647
pdef,str-v,s,x
plpath,str-v
/show,str-v
plpath,str-v
/show,unused
/show,x11
FINISH
/EXIT
```

A.4.2 Input Listing for Modal Analysis

Processes of inputting material data, generating the solid model and meshing are as same as the static analysis. So we can use "resume" command to recover the meshed solid model.

```
/COM, RECOVER THE MESHED SOLID MODEL
/show,x11
/menu,on
RESUME

/PREP7
/COM, DEFINE THE MASS ELEMENT OF ZERO
et,2,mass21
etlist
r,1,0.0
type,2
e,663

/COM, DEFINE DEGREE OF FREEDOM ON THE MASTER NODES FOR OUTPUT
NSEL,S,LOC,Z,3.5e-4,4.0e-4
nplot
M,P50X,UZ 605
M,P50X,UZ 604
M,P50X,UZ 603
M,P50X,UZ 602
M,P50X,UZ 601
M,P50X,UZ 600
M,P50X,UZ 599
M,P50X,UZ 598
M,P50X,UZ 597
M,P50X,UZ 596
M,P50X,UZ 595
M,P50X,UZ 606
M,P50X,UZ 610
M,P50X,UZ 609
M,P50X,UZ 608
M,P50X,UZ 607
M,P50X,UZ 612
M,P50X,UZ 611
M,P50X,UZ 659
M,P50X,UZ 695
M,P50X,UZ 696
M,P50X,UZ 691
M,P50X,UZ 692
M,P50X,UZ 693
M,P50X,UZ 694
M,P50X,UZ 690
M,P50X,UZ 679
M,P50X,UZ 680
M,P50X,UZ 681
```

```
M,P50X,UZ 682
M,P50X,UZ 683
M,P50X,UZ 684
M,P50X,UZ 685
M,P50X,UZ 686
M,P50X,UZ 687
M,P50X,UZ 688
M,P50X,UZ 689
nsel,all,all
SAVE
FINISH

/SOLU

/COM, DEFINE THE ANALYSIS TYPE
ANTYP,2
MODOPT,REDU, 3, 0. ,1000000.0 , 3,OFF
SOLVE
FINISH

/COM, POSTPROCESS
/POST1
set,1,1
pldisp,2
/show,f11
pldisp,2
/show,x11
set,1,2
pldisp,2
/show,f12
pldisp,2
/show,x11
set,1,3
pldisp,2
/show,f13
pldisp,2
/show,x11
FINISH

/PREP7
/COM, DEFINE THE MASS ELEMENT OF 0.586 ng
rdele,all
rlist
r,1,0.586e-9,0.586e-9,0.586e-9_
type,2
```

e,663
SAVE
FINISH
/SOLU
SOLVE
/COM, REPEATING THE PROCESS MENTIONED ABOVE WITH DIFFERENT MASS VALUE, WE CAN GET THE SHIFT IN THE RESONANT FREQUENCY AS A FUNCTION OF THE LOADED MASS.

A.4.3 Input Listing for Reduced Harmonic Analysis

/COM,ANSYS REVISION 5.0 24 13:46:46 12/28/1994
/show,x11
/menu,on
RESUME
/PREP7
VLIST
VGEN,2,1,81,,,0.01,,1000,0 --- To generate another solid model of cantilever
nplot
nlist
mlist
/COM, DEFINE THE MASTER NODES ON THE NEW SOLID MODEL
mgen,2,1736,595,612
mgen,2,1736,659
mgen,2,1736,679,696
/COM, LOAD A SPHERE ON ONE CANTILEVER TIP
rdele,all
r,1,0.586e-9,0.586e-9,0.586e-9
type,2
e,663
save
FINISH
/SOLU
ddele,all,all
/COM, DEFINE THE BOUNDARY CONDITIONS
nsel,s,loc,x,-0.001,0.1e-4
nplot
d,all,all,0.0
nsel,all
save
/COM, MODAL ANALYSIS FIRST. IT IS NECESSARY
ANTYPE, MODAL
MODOPT, REDUC

```
SOLVE
/post1
set,1,1
pldisp,2 --- You can see the fundamental mode shape of one cantilever
set,1,2
pldisp,2 --- You can see the fundamental mode shape of another cantilever
set,1,3
pldisp,2 --- You can see the first torsion mode shape of the cantilever
FINISH
/COM, REDUCED HARMONIC ANALYSIS
/SOLU
ANTYPE,HARM
HROPT,MSUP
HROUT,ON
HARFRQ,3500,5500
NSUBST,200
KBC,1
DMPRAT,0.03
f,695,fz,0.002
f,611,fz,0.002
f,2431,fz,0.002
f,2347,fz,0.002
solve
FINISH
/COM, POSTPROCESS
/POST26
file,,rfrq
nsol,2,695,u,z,load
nsol,3,2431,u,z,no-load
plvar,3,2
/show,f-shift
plvar,3,2
/show,x11
FINISH
```

Appendix B:

Electrical Properties of the Polysilicon Film

A polycrystalline material is composed of small crystallites joined together by grain boundaries. The angle between the orientations of the adjoining crystallites is often large. Inside each crystallite the atoms are arranged in a periodic manner so that it can be considered as a small single crystal. The grain boundary is a complex structure, usually considering of a few atomic layers of disordered atoms. Atoms in the boundary represent a transitional region between the different orientations of neighboring crystallites. There are two proposed mechanisms describing the effects of the grain boundary upon the electrical properties of doped polycrystalline semiconductors. First one [20] suggests that the grain boundary acts as a sink for impurity atoms due to impurity segregation at the grain boundary. So, the amount of impurity in the crystalline is reduced, which leads to a much smaller carrier concentration than the uniformly distributed impurity concentration. The carrier concentration does not approach that of the doping concentration until the grain boundary is saturated with impurity atoms. It was also suggested that the segregation of the impurity caused the grain interiors to have higher resistance than the grain boundaries. However, it has been shown that segregation of boron at the grain boundary is significant only at extremely heavily doped concentrations of silicon (1.3 at percentage of boron). No segregation was observed for doping as high as 1.3×10^{20} /cm^3. If the reduction of carriers is the result of impurity segregation at the grain boundary, it is expected that the carrier concentration reduction would depend on the impurity element. But it was observed [21] that both boron and phosphorus behaved similarly in polysilicon. It is also difficult to explain how impurity segregation can lead to the mobility minimum seen in the experi-

ments [22, 23].

The second mechanism [22, 23] suggests that since the atoms at the grain boundary are disordered, there are a large number of defects due to incomplete atomic bonding. This results in the formation of trapping states. These trapping states are capable of trapping carriers and thereby immobilizing them. This reduces the number of free carriers available for electrical conduction. After trapping the mobile carriers the traps become electrically charged, creating a potential energy barrier which impedes the motion of carriers from one crystallite to another, thereby reducing their mobility. Based on this model, for the same amount of doping, the mobility and carrier concentration of a polycrystalline semiconductor would be less than that of a single-crystalline material.

Based on the assuming that the electrical transport properties of polysilicon films are mainly governed by carrier trapping at the grain boundary, the carrier movement in the applied electrical field can be described with Poisson's equation, and the I-V characteristics, the carrier concentration and resistivity can be expressed [22, 23, 24]. The real polysilicon material is a three-dimensional substance. It can be assumed that polysilicon is composed of identical cubic crystallites with a grain size L cm and a boundary thickness δ. Its transport properties can be considered as one-dimensional, seen in Figure B.1. It is also assumed that there is only one type of impurity atom present, and the impurity atoms are totally ionized and uniformly distributed with a concentration of N cm^{-3}. For this structure, Poisson's equation becomes

$$\frac{d^2V}{dx^2} = \frac{-qN}{\epsilon} \qquad l < |x| < \frac{L}{2} \tag{8}$$

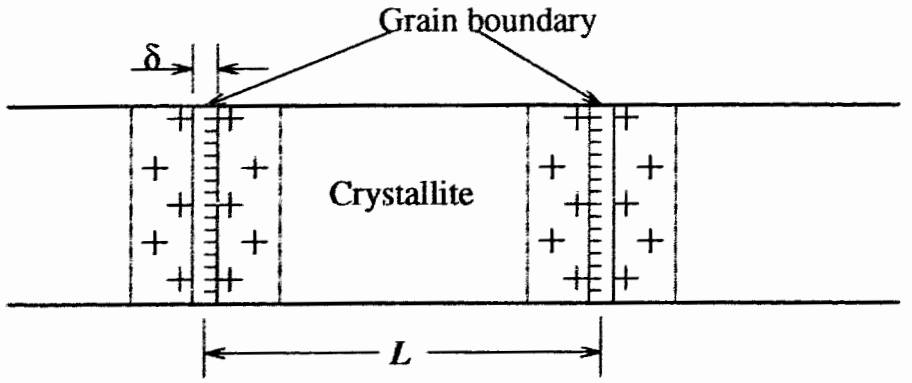

(a) Crystal Structure

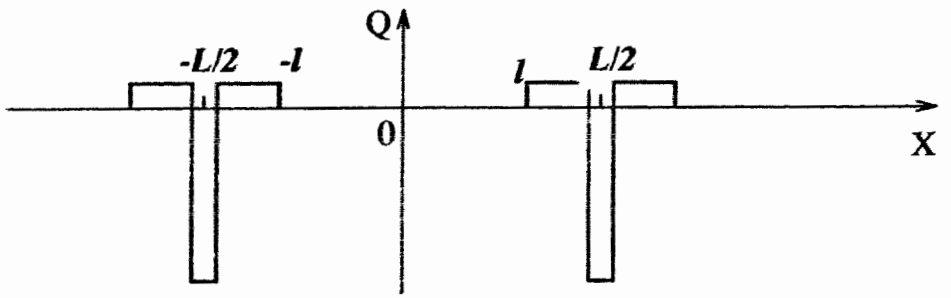

(b) Charge Distribution

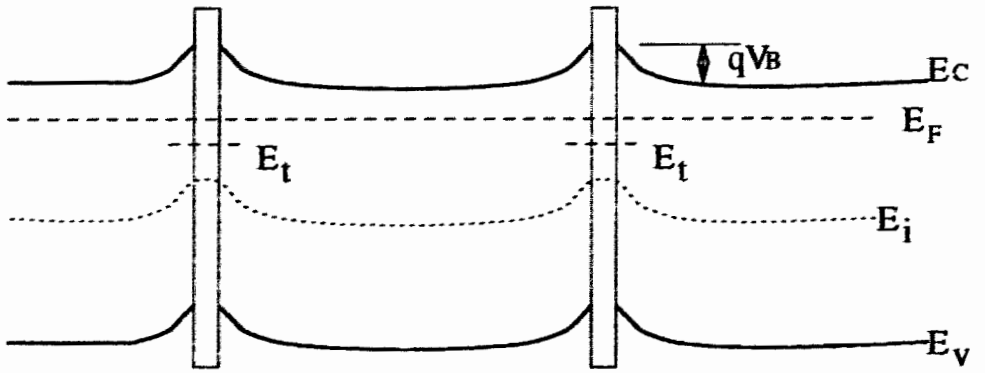

(c) Energy-band Diagram for N-type Dopants

(d) Grain Boundary and Crystallite Resistivity Model

Figure B.1: Analysis model of polysilicon film

where ε is the dielectric permittivity of polysilicon. Integrating this equation and applying the boundary conditions that $V(x)$ is continuous and dV/dx is zero at $x=l$ gives

$$V(x) = (-\frac{qN}{2\varepsilon})(x-l)^2 + V_0 \qquad l < |x| < \frac{L}{2} \tag{9}$$

where V_0 is the potential at the center of the crystallite. In this solution, the Fermi level is taken to be same in the every region.

For a given crystallite size, there exist two possible conditions depending on the doping concentration: (a) $LN<Q_t$, and (b) $LN>Q_t$.

We first consider the case for $LN<Q_t$. Under this condition, the crystallite is completely depleted of carriers and the traps are partially filled, so that $l = 0$ and $V(x)$ becomes

$$V(x) = -\frac{qN}{2\varepsilon}x^2 + V_0 \qquad |x| < \frac{L}{2} \tag{10}$$

The potential barrier height, V_B, is the difference between $V(0)$ and $V(L/2)$, i. e.,

$$V_B = \frac{qL^2N}{8\varepsilon} \tag{11}$$

showing that V_B increases linearly with N. Using Boltzmann statistics, the mobile carrier concentration, $n(x)$, becomes

$$n(x) = N_C \exp\{-\frac{[qV(x) - E_F]}{kT}\} \tag{12}$$

where N_C is the effective density of states in the conduction band and E_F is the Fermi level. The average carrier concentration, N_a, is obtained by integrating n(x) from $-L/2$ to $L/2$ and dividing by the grain size. The result is

$$N_a = \frac{n_i}{Lq}\left(\frac{\pi 2\varepsilon kT}{N}\right)^{1/2} \exp\left(\frac{qV_b + E_F}{kT}\right) \operatorname{erf}\left(\frac{qL}{2}\left(\frac{N}{2\varepsilon kT}\right)^{1/2}\right) \tag{13}$$

where n_i is the intrinsic carrier concentration of single-crystalline silicon. The Fermi level can be determined by equating the number of carriers trapped to the total number of trapping states occupied, given as

$$LN = \frac{Q_t}{2\exp\left[-\frac{(E_t - E_F)}{kT}\right] + 1} \tag{14}$$

From this equation, Fermi level is given as

$$E_F = E_t + kT\ln\left(\frac{1}{2}\left(\frac{Q_t}{LN} - 1\right)\right) \tag{15}$$

With Eqs. (13) and (15), the carrier concentration can be calculated for a given N, if L, Q_t, and E_t are known.

If $LN > Q_t$, only part of the crystallite is depleted of carriers and $l > 0$. The potential barrier height then becomes

$$V_B = q\frac{Q_t^2}{8\varepsilon N} \tag{16}$$

Based upon Eqs. (11) and (16), the grain boundary potential barrier is a function of the doping concentration. It is noted that as the doping concentration is increased, the potential barrier at first increases linearly, reaching a maximum at $LN = Q_t$, then decreases rapidly as $1/N$. In the undepleted region, the carrier concentration, n_b, is the same as that of a similarly doped single-crystalline silicon,

$$n_b = N_C\exp\left(\frac{E_C(0) - E_F}{kT}\right) \tag{17}$$

for a nondegenerately doped sample. The carrier concentration in the depletion region is given in Eq.(12). The average carrier concentration, n_a, can be written as

$$n_a = n_b \{ (1 - \frac{Q_t}{LN}) + \frac{1}{qL} (\frac{2\varepsilon kT\pi}{N})^{1/2} \text{erf} (\frac{qQ_t}{2} (\frac{1}{2\varepsilon kTN})^{1/2}) \} \quad (18)$$

The resistance of a polycrystalline material consists of the contributions from the grain-boundary region and the bulk of the crystallite. If the conductivity in the crystallite is much higher than that through the grain boundary, it is a good approximation to consider just the resistance of the grain-boundary region. There are two important contributions to the current across the grain boundary: thermionic emission and tunneling (field emission). Thermionic emission results from those carriers possessing high enough energy to surmount the potential barrier at the grain boundary. On the other hand, the tunneling current arises from carriers with energy less than the barrier height. These carriers go through the barrier by quantum-mechanical tunneling.

When the barrier is narrow and high, the tunneling current can become comparable to or larger than the thermionic emission current. In polysilicon the potential barrier is higher when the barrier width becomes wider. The barrier height decreases rapidly to a small value for a highly doped polysilicon, therefore, the tunneling current is always expected to be smaller than the thermionic emission current. Because of this, the tunneling current will be neglected in our calculation, for the polysilicon gate material of commercial CMOS technology usually is heavily doped (1.9×10^{19} /cm^3 for 4000Å polysilicon with sheet resistance 20 Ω).

The thermionic-emission theory for an applied voltage, V_a, across a grain boundary demonstrates [25] that

$$J_{th} = qn_b\left(\frac{kT}{2\pi m^*}\right)^{1/2} \exp\left(-\frac{qV_B}{kT}\right)\left(\exp\left(\frac{qV_a}{kT}\right) - 1\right) \tag{19}$$

where m^* is the effective mass of the carrier. If V_a is small, $qV_a \ll kT$, it can be expanded to give

$$J_{th} = q^2 n_b\left(\frac{1}{2\pi m^* kT}\right)^{1/2} \exp\left(-\frac{qV_b}{kT}\right) V_c \tag{20}$$

which is a linear current-voltage relationship. From this equation, the barrier resistivity ρ_B (defined as the electric field divided by current density) is

$$\rho_B = \frac{V_a}{J(L-2l)} = \frac{1}{(L-2l)q^2 n_b}(2\pi m^* kT)^{1/2} \exp\left(\frac{qV_B}{kT}\right) \tag{21}$$

Similarly, crystallite bulk resistivity is

$$\rho_C = \frac{V_C}{(2l)J} \tag{22}$$

where V_C is the voltage across the crystallite neutral region. Total resistivity ρ, which includes ρ_B and ρ_C, is

$$\rho = \frac{V_a + V_C}{JL} = \rho_B(\frac{L-2l}{L}) + \rho_C(\frac{2l}{L}) \tag{23}$$

From the above analysis, it can be summarized as: (a)when the doping level is lower, the depletion layer at the grain boundary is wider, therefore, the grain boundary resistivity is main part, and the function of ρ_B is reducing as the doping level is increased (the polysilicon with very heavily doping has the almost same resistivity value as the single-crystalline silicon with the same amount of doping [22, 23]); (b)since $\rho_B \propto \frac{T^{1/2}}{n_i}\exp(\frac{qV_B}{kT})$, at lower doping level, the resistivity decreases as the temperature increases, and this effect is getting weaker as the doping is increased (it was observed in the experiments [22, 23]).

In bulk silicon the change in conductivity is due to a shift in the relevant conduction and valence band minima and maxima relative to each other, resulting in a redistribution of the carriers between the minima or bands. The transport of carriers across the barrier is assumed to be dominated by the thermionic emission and total current has a contribution from each minima. A shift in these minima relative to each other will result in a change in their relative contribution to the thermionic emission and thus a change in the conductivity of the barrier. So the piezoresistance in polysilicon incorporates both barrier and bulk effects.

The polysilicon film consists of grains of length L, separated by negligibly thin grain boundary of thickness δ. A depletion region of depth $w = \frac{L}{2} - l$ into the grain is devel-

oped due to the trapping of carriers at the boundary. Thus the total resistivity of the polysilicon can be given as Eq. (23).

The gauge factor G of a material is defined as the fractional change in resistance per unit strain

$$G = \frac{\Delta R}{R\zeta} \tag{24}$$

where ζ is the applied strain. Consider a resistor of dimensions x, y, z with a resistivity ρ. The resistance is thus given by:

$$R = \frac{x\rho}{yz} \tag{25}$$

The fractional change in resistance can be calculated by differentiating this equation, yielding

$$\frac{\Delta R}{R} = \frac{\Delta x}{x} - \frac{\Delta y}{y} - \frac{\Delta z}{z} + \frac{\Delta \rho}{\rho} \tag{26}$$

If a uniaxial stress, $\sigma_{x'x'}$, is applied to the resistor at an angle η to the current flow, then

the strain $\zeta_{x'x'}$ must be resolved as shown in Figure B.2. The resulting components of the strain are given by [26]:

$$\begin{aligned}
\zeta_{xx} &= \zeta_{x'x'}\cos^2\eta + \zeta_{z'z'}\sin^2\eta - \frac{1}{2}\gamma_{x'z'}\sin 2\eta \\
\zeta_{zz} &= \zeta_{z'z'}\cos^2\eta + \zeta_{x'x'}\sin^2\eta + \frac{1}{2}\gamma_{x'z'}\sin 2\eta \\
\gamma_{xz} &= \sin 2\eta\,(\zeta_{x'x'} - \zeta_{z'z'}) + (\cos^2\eta - \sin^2\eta)\,\gamma_{x'z'} \\
\zeta_{yy} &= \zeta_{y'y'}
\end{aligned} \tag{27}$$

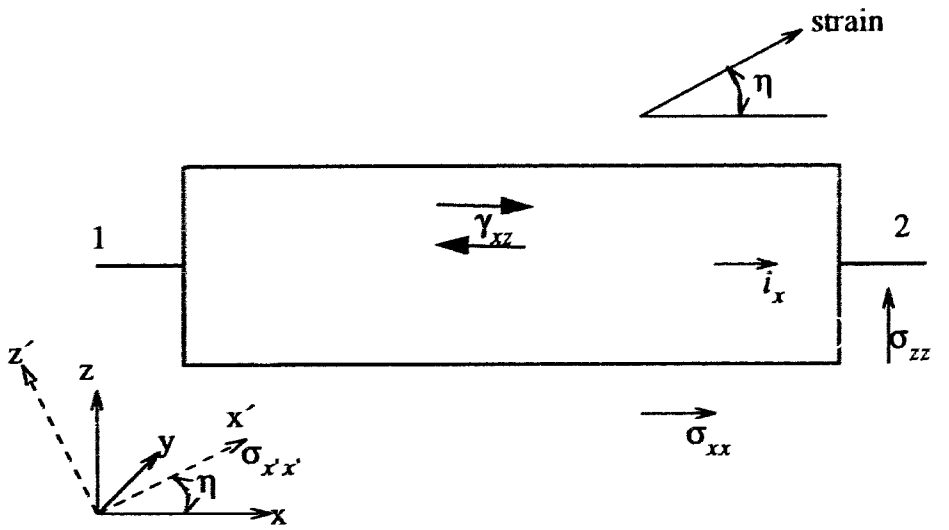

Figure B.2: Two terminal resistor with an applied stress at an angle η to the current flow

In the case of a uniaxially applied stress the shear component $\gamma_{x'z'}$ is zero, thus substitut-

ing equation (27) in equation (26) yields

$$\frac{\Delta R}{R} = (\cos^2\eta - \sin^2\eta)\,(\zeta_{x'x'} - \zeta_{z'z'}) - \zeta_{y'y'} + \frac{\Delta\rho}{\rho} \tag{28}$$

The first two terms results from the change in the body size of the resister under the applied stress. For a special case of $\eta = 0°$ (it is the case that the first two terms have biggest value), this equation will become

$$\frac{\Delta R}{R\zeta_{x'x'}} = 1 + \nu_{x'z'} + \nu'_{x'y'} + \frac{\Delta\rho}{\rho\zeta_{x'x'}} \tag{29}$$

For the special case of $\eta = 45°$, Equ. (29) becomes

$$\frac{\Delta R}{R\zeta_{x'x'}} = \nu_{x'y'} + \frac{\Delta\rho}{\rho\zeta_{x'x'}} \tag{30}$$

where $\nu_{x'y'}$, $\nu_{x'z'}$ are Poisson's ratios relating to the reduction in the film thickness due to strain. The additional effect of shear, γ_{xz}, on the resistance of the device is a second-order effect and is not included in this model. For silicon, the Poisson's ratio is 0.09 [14]. From the equations (29) and (30), the deformation of the resistor size has a biggest contribution of 1.09 to the gauge factor. For silicon or polysilicon material, the experimental gauge fac-

tor can range from 15 to 27 [9, 10]. Therefore, the contribution of the change in the size of the resistor to the gauge factor is negligible. The main contribution is the resistivity change of the polysilicon. The last term of equation (29) or (30) describes the fractional change in resistivity. The polysilicon film is assumed to have grains of size L, separated by a negligibly thin grain boundary of thickness δ (which is of the order of 1 nm). A depletion width, $w = \frac{L}{2} - l$, into the grain is developed due to the trapping of carriers at the boundary. Since the fraction of the applied voltage across each barrier of the grain boundary is small ($V_a \ll \frac{kT}{q}$) the barrier can be modelled as a linear resistor. Therefore the resistivity of the film can be given by equation (23). In order to find the fractional change in the resistivity, equation (23) is differentiated, thus yielding

$$\frac{\Delta\rho}{\rho} = \frac{\Delta\rho_B (L-2l)}{\rho L} + \frac{\Delta\rho_C 2l}{\rho L} \tag{31}$$

Thus the resistivity change for one grain is given by [27]:

$$\frac{\Delta\rho}{\rho\zeta} = \frac{\rho_B \pi'_{srB} / S'_{ii}}{\rho_B + \rho_C (2l)/(L-2l)} + \frac{\rho_C \pi'_{srC} / S'_{ii}}{\rho_C + \rho_B (L-2l)/(2l)} \tag{32}$$

where π'_{srC} and π'_{srB} are the effective piezoresistive coefficients of the undepleted grain and barrier regions respectively, and S'_{ii} is the compliance coefficient for a strain parallel to stress, and it has the value of Young's modulus. π'_{srC} is given by

$$\frac{\pi'_{srC}}{S'_{ii}} = \cos^2\eta \frac{\pi'_{11C}}{S'_{ii}} + \sin^2\eta \frac{\pi'_{12C}}{S'_{ii}} + \frac{1}{2}\sin 2\eta \frac{\pi'_{16C}}{S'_{ii}} \tag{33}$$

where π'_{11C}, π'_{12C} and π'_{16C} are piezoresistive coefficients after the axis system is rotated and can be expressed in terms of the standard piezoresistive coefficients π_{11}, π_{12} and π_{44} of the single-crystalline silicon by:

$$\begin{aligned}
\pi'_{11} &= \pi_{11} + 2(\pi_{12} + \pi_{44} - \pi_{11})\,(l_1^2 m_1^2 + l_1^2 n_1^2 + n_1^2 m_1^2) \\
\pi'_{12} &= \pi_{12} + (\pi_{11} - \pi_{12} - \pi_{44})\,((l_1^2 l_2^2 + m_1^2 m_2^2 + n_1^2 n_2^2)) \\
\pi'_{16} &= 2(\pi_{11} - \pi_{12} - \pi_{44})\,(l_1^3 l_2 + m_1^3 m_2 + n_1^3 n_2)
\end{aligned} \tag{34}$$

The axis rotation is defined by the direction cosines l_i, m_i and n_i by the following matrix:

$$\begin{bmatrix} x' \\ y' \\ z' \end{bmatrix} = \begin{bmatrix} l_1 & m_1 & n_1 \\ l_2 & m_2 & n_2 \\ l_3 & m_3 & n_3 \end{bmatrix} \begin{bmatrix} x \\ y \\ z \end{bmatrix} \tag{35}$$

The effective piezoresistive coefficient in barrier region π'_{srB} can be expressed with a similar equation as equation (33) in terms of the barrier piezoresistive coefficients π'_{11B}, π'_{12B} and π'_{44B}, [28, 29].

The grain boundary can be modelled on a Schottky-type barrier with a conductivity contri-

bution, σ_i, from the ith valley in n-type material expressed as

$$\sigma_i \propto m_i^* \exp(-q\frac{V_B}{kT})\exp(-\frac{E_i - E_F}{kT}) \tag{36}$$

where qV_B is the barrier height, E_i is the energy of the ith valley minima, E_F is the Fermi energy and m_i^* is the effective mass contribution from the ith valley. When there is a strain acting on the grain boundary, the conductive contribution of each valley to the thermionic emission from within the grain will change due to the band minima energy shift. On the assumption that the barrier height is unaffected by the strain, that the bands are not distorted and that the total number of carriers is constant, the piezoresistive coefficients can be derived as [29]

$$\begin{aligned} \pi_{11B} &= \frac{2\Xi_u (m_{100}^* - m_{010}^*)\ (S_{11} - S_{12})}{3kT\,(m_{100}^* + 2m_{010}^*)} \\ \pi_{12B} &= -\frac{\Xi_u (m_{100}^* - m_{010}^*)\ (S_{11} - S_{12})}{kT\,(m_{100}^* + 2m_{010}^*)} \\ \pi_{44B} &= 0 \end{aligned} \tag{37}$$

where Ξ_u is the deformation potential constant, m_{100}^* is the effective mass contribution from the (100) valley, S_{11} and S_{12} are the compliance coefficients for a strain parallel to

stress and for a strain perpendicular to stress, respectively.

Putting equations (32) and (29) into equation (24), we can get the single grain gauge factor as:

$$G_s = \frac{\Delta R}{R\xi} = (\cos^2\eta - \sin^2\eta)\,(1+\nu_{x'y'}) + \nu_{x'z'} + \frac{\rho_B \pi'_{srB}/S'_{ii}}{\rho_B + \rho_C (2l)/(L-2l)} + \frac{\rho_C \pi'_{srC}/S'_{ii}}{\rho_C + \rho_B (L-2l)/(2l)} \tag{38}$$

The polysilicon film structure can consist of crystallites with a random distribution. In this case, the gauge factor can be estimated by averaging equation (38) over all possible directions. This results in the equation

$$G = (\cos^2\eta - \sin^2\eta)\,(1+\nu) + \nu + \langle (R_1 \pi'_{srB}/S'_{ii}) + (R_2 \pi'_{srC}/S'_{ii}) \rangle \tag{39}$$

where

$$R_1 = \frac{\rho_B}{\rho_B + \rho_C (2l)/(L-2l)}$$
$$R_2 = \frac{\rho_C}{\rho_C + \rho_B (L-2l)/(2l)} \tag{40}$$

and

$$\langle (R_1\pi'_{srB}/S'_{ii}) + (R_2\pi'_{srC}/S'_{ii}) \rangle =$$

$$\frac{\int_{\vartheta=0}^{\pi/2}\int_{\phi=0}^{\pi/4} \left((R_1\pi'_{srB}/S'_{ii}) + (R_2\pi'_{srC}/S'_{ii}) \right) d\theta d\phi}{\int_{\theta=0}^{\pi/2}\int_{\phi=0}^{\pi/4} d\theta d\phi|_{\psi=0}} \qquad (41)$$

REFERENCES

[1] E. Bassous, H. H. Taub, and L. Kuhn, "Ink jet printing nozzle arrays etched in silicon", Appl. Phys. Lett., vol. 31, p. 135 (1977)

[2] A. C. M. Gieles, and G. H. J. Somers, "Miniature pressure transducers with silicon diaphragm", Philips Tech. Rev., Vol. 33, 1973, P14

[3] L. M. Roylance, and J. B. Angell, "A batch-fabrication silicon acceierometer", IEEE Trans. Electron Devices, Vol. ED-26, No. 12, P1911-1917, 1979

[4] R. T. Howe, "Surface micromachining for microsensors and microactuators", J. Vac. Sci. Technol. B, Vol. 6, No. 6, P1809-1813, 1988

[5] M. Parameswaran, H. P. Baltes, Lj. Ristic, A. C. Dhaded and A. M. Robinson, "A new approach for the fabrication of micromechanical structures", Sensors and Actuators, 19 (1989), 289-307

[6] M. Parameswaran, Lj. Ristic, A. M. Robinson, K. Chau and W. Allegretto, "Electrothermal Microactuators in standard CMOS process", Sensors and Materials, 2, 4 (1991) 197-205

[7] M. Parameswaran, A. M. Robinson, Lj. Ristic, K. Chau and W. Allegretto, "A CMOS thermally isolated gas flow sensor", Sensors and Materials, 2, 1 (1990) 17-26

[8] S. Prescesky, M. Parameswaran, A. Rawicz, R. F. B. Turner and U. Reichl, "Silicon micromachining Technology for sub-nanogram discrete mass resonant biosensors", Canadian J. Phys., Vol. 70, P1178, 1992

[9] John Y. W. Seto, "Piezoresistive properties of polycrystalline silicon", J. Appl. Phy., Vol.47, N0. 11, 4780-4783 (1976)

[10] J. C. Erskine, "Polycrystalline silicon-on-metal strain gauge transducers", IEEE Trans. on Electron Devices, Vol. ED-30, No. 7, P796-801 (1983)

[11] E. Lüder, "Polycrystalline silicon-based sensors", Sensors and Actuators, 10 (1986), P9-23

[12] T. Boltshauser, A. Häberli and H. Baltes, "Piezoresistive membrane hygrometers based on IC technology", Sensors and Materials, 5, 3(1993) P125-134

[13] R. J. Stephenson, "Mechanics and Properties of Matter", 2nd edition, John Willy & Sons, 1964.

[14] K. E. Petersen, "Silicon as a mechanical material", Proc. of IEEE, Vol. 70, No. 5, (1982), P420.

[15] S. B. Prescesky, "Micromachined discrete mass resonant sensors", Thesis of M. Ap. S., Simon Fraser University, Canada, 1992

[16] M. Parameswaran, D. Xie and P. Glavina, "Fabrication of nickel micromechinical structures using a simple low-temperature electroless plating process", J. Electro. Chemical Society, Vol. 140, No. 7, 1993, P111-113

[17] W. T. Thomsom, "Theory of Vibration with Application", 2nd ed., Englewood Cliffs: Prentice-Hall Inc., 1981

[18] K. K. Frame and W. Hu. "Cell volume measurement as an estimation of mammalian cell biomass", Biotechnology and Bioengineering, 36 (1990), P191-197

[19] D. G. Kilburn, P. Fitzpatrick, B. C. Blake-Coleman, D. J. Clarke and J. B. Griffiths, "On-line monitoring of cell mass in mammalian cell cultures by acoustic densitometry", Biotechnology and Bioengineering, 33 (1989), 1379-1384

[20] M. E. Cowher and T. O. Sedgwick, "Chemical vapor deposited polycrystalline silicon", J. Electrochem. Soc., 119 (1972), P1565

[21] T. I. Kamins, "Hall mobility in chemically deposited polycrystalline silicon", J. Appl. Phy. 42 (1971), P4357

[22] John Y. W. Seto, "The electrical properties of polycrystalline silicon films", J. Appl. Phy. 46 (1975), P5247

[23] N. C. C. Lu, L. Gerzberg, C. Y. Lu and J. D. Meindl, "Modeling and optimization of monolithic polycrystalline silicon resistors", IEEE ED-28, No. 7 (1981), P818

[24] P. Rai-Choudhury and P. L. Hower, "Growth and characterization of polycrystalline silicon", J. Electrochem. Soc. 120 (1973), P1761

[25] S. M. Sze, Physics of Semiconductor Devices, New York: Wiley, 1981

[26] J. W. Dally and W. F. Riley, Experimental Stress Analysis, McGraw-Hill/Kogakushu Ltd., Tokyo, 1978, P26-45

[27] P. J. French and A. G. R. Evans, "Polysilicon strain sensors using shear piezoresistance", Sensors and Actuators, A 15 (1988), P257-272

[28] P. J. French and A. G. R. Evans, "Polycrystalline silicon as a strain gauge material", J. Phys. E. 19 (1986), P1055-1058

[29] P. J. French and A G. R. Evans, "Polycrystalline silicon strain sensors", Sensors and Actuators, 8 (1985), P219-225